ISSN 1812-1195 (Print)
ISSN 2618-0596 (Online)

IRAQI JOURNAL OF LASER

A refereed scientific journal issued by
Institute of Laser for Postgraduate Studies, University of Baghdad

Volume 21
Issue (2) 2022

جامعة بغداد

المجلّة العراقية للّيزر

علمية متخصصة محكّمة

المجلد 21

الأصدار الثاني 2022

تصدر عن معهد الليزر للدراسات العليا / جامعة بغداد

IRAQI JOURNAL OF LASER

VOLUME 21 Issue (2) 2022

Contents

Iraqi J. Laser, issue 2, vol., 21, pp. 1-8 (2022)

IRAQI JOURNAL OF LASER

Biosensing technique for detection of H.pylori bacteria

Israa M.L. SaQari, Layla M.H. Al-ameri

**Corresponding author: biologist.israa@gmail.com*

Institute of Laser for Postgraduate Studies, University of Baghdad, Baghdad, Iraq

(Received 22/4/2022; accepted 7/8/2022)

Abstract: ***H.pylori*** is an important cause of gastric duodenal disease, including gastric ulcers, Mucosa-associated lymphoid tissue (MALT), and gastric carcinoma. biosensors are becoming the most extensively studied discipline because the easy, rapid, low-cost, highly sensitive, and highly selective biosensors contribute to advances in next-generation medicines such as individualized medicine and ultrasensitive point-of-care detection of markers for diseases. Five of ten patients diagnosed with *H.pylori* ranging in age from 15–85 participated in this research. who [gastritis, duodenitis, duodenal ulcer (DU), and peptic ulcer (PU)] Suspected *H.pylori* colonies were identified by the presence of urease, catalase, oxidase activity, and PCR. All parameters are fixed: Laser power:40 mW, size of drops:25 µ, Turbidity:0.5. , Multi modes optical fiber, and Coreless optical fiber to construct optical biosensor (Multimode-Coreless-Multimode) optical fibers based on an inline Mach-Zehnder Interferometer. All samples had a sensitivity. Multimode-Coreless-Multimode optical Biosensor: is a rapid and sensitive method for the detection of *H.pylori* bacteria.

Keywords: Helicobacter pylori (H. pylori); Bacteria; bacterial detection; Optical Biosensor;

Introduction

H.pylori may infect the human stomach. It was first recognized in 1983 as playing a role in human illness. Bacteria are found in the stomach's inner wall and cause inflammation. infection Unless treated with eradication drugs, it seems to last a lifetime (Yamaoka and Graham, 2013). *H.pylori* infection always causes active chronic gastritis. This can be clinically overlooked throughout life in most people, but in a significant minority, gastroduodenal disease, especially digestive ulcer disease, cardia-free gastric cancer, and Mucosa-associated lymphoma tissue (MALT). To prevent and control bacteria in the environment, it is essential to create accurate, effective, and rapid methods for detecting bacteria (Cheng Y, 2017). During the last century, a range of methods for detecting bacteria was developed. Traditional culture methods, immunological techniques, molecular biology techniques, and biosensors are all types of these (Koyun, Ahlatcolu and Koca, 2012).Because of their proven high efficiency, biosensors are one of the most important technologies. Low cost, fast response, high sensitivity, and high selectivity (Ra *et al.*, 2012). Biosensors act by sensing target

molecules with biological materials (like antibacterial peptides, lectins, antibodies, and amplifiers, and signal processors are all examples of biosensor components (Pandey *et al.*, 2017). A detectable signal, such as an electrical or optical signal, is generated and detected by the transducer when a biological component detects an analyte and produces a catalytic or binding event (Usman *et al.*, 2019). The signal is proportional to the analyte concentration, Response time, dynamic range, detection limit, single-to-noise ratio, and specificity are all that affect biosensor performance. (Bobrinetskiy *et al.*, 2021). Biological detection elements, transducers, and signal amplifiers are all closely related to these elements. It is the most crucial part of biosensors (Monošík, Streďanský and Šturdík, 2012)Biosensors provide a fast and inexpensive way to detect bacteria and provide measurable or detectable readings. A biosensor is a method of visual, mechanical, or electrical means of communication and the receptors used (ie, catalyst [enzyme] or affinity-based [antibody, aptamer, lectin, bacteriophage]. Etc.), which can be categorized in different ways . In general, Biosensors have been developed for a variety of analytes, from single ions and small molecules to nucleic acids and proteins, viruses, and whole bacteria.This study aims to identify *H.pylori* isolated from Iraqi patients' clinical specimens before developing a new form. Using biosensors and their operating principles provides accurate, rapid, and practical detectors.

Materials and methods

In an ordinary method for isolation of *H.pylori* from patients, the sample was taken before proton pump inhibitor (PPI) ingestion of antibiotic therapy and directed endoscopy, and at least two simultaneous gastric mucosal biopsies were obtained approximately 3 cm from each patient-guided gastric duodenum. (One from the sinus and the other from the patient's stomach). Endoscopy (OGD) of the upper esophagus (OGD) under the supervision of an endoscopist with standard biopsy forceps using xylose as local anesthesia assesses the degree of clinical condition and A biopsy was performed immediately to determine the presence of aptamers) and generating detectable signals. Biological sensor elements, transducers, signal *H.pylori*. The culture is analyzed and processed as soon as possible, placed in the appropriate transport. Ideally, Within 6 hours for *H.pylori* isolation and identification. The biopsy was first ground with 0.5 ml burusera broth with an electric homogenizer. The suspension was then plated on a BHI broth medium. Columbia Blood Agar (10 mg / ml) enriched with 10% human blood and supplemented with vancomycin (10 mg / ml), ceftaroline (5 mg / ml), trimethoprim (5 mg- / ml) and action (100 mg / ml). After 24 hours in Himedia), the plates were incubated in a slightly anaerobic atmosphere (glass containing GasPaks) for 2 days. Suspected *H.pylori* colonies were identified by the presence of urease, catalase, oxidase activity, and PCR. In this work Multimode – Coreless –multimode (MCM) types of the optical biosensor are used to detect the *H.pylori* bacteria as shown in figure(1)based on inline Mach-Zehnder interference. The Multimode fiber (50 /125μm) core/cladding diameter and Coreless fiber (125μm) cladding diameter have the same procedure of fabrication. In which use optical fiber stripping tools to remove the coating for 2 cm long. The optical fiber stripper has three holes. The first hole is used for stripping the (1600-3000) μm, the second hole is used for striping the coating buffer of (600-900) μm, and the last hole is used to remove the acrylate coating of (250 μm) thickness. After removing the outer coating to obtain a flat edge of the fiber with 90 angles flat surface the cleaver machine(Fiber cleaver X-50C) By placing the fiber optic's edge on the cleavage machine's cutting blade, a perfectly smooth final edge is obtained. Use alcohol or a damp cloth to clean the fibers of the remaining coating. If the tip of the fiber does not cleave smoothly, the fiber needs to be cleaved again After we get a flattened edge of the fiber we use a Fusion splicing machine (Fusion splicer S-16)as shown in figure(2) MCM optical fiber 30cm in length was considered as the conventional optical fiber, a segment about 3 cm in length was made in the middle of the fiber using a cutter to make a .The whole fiber (30) cm was put on the plate using adhesive as shown in figure (3).

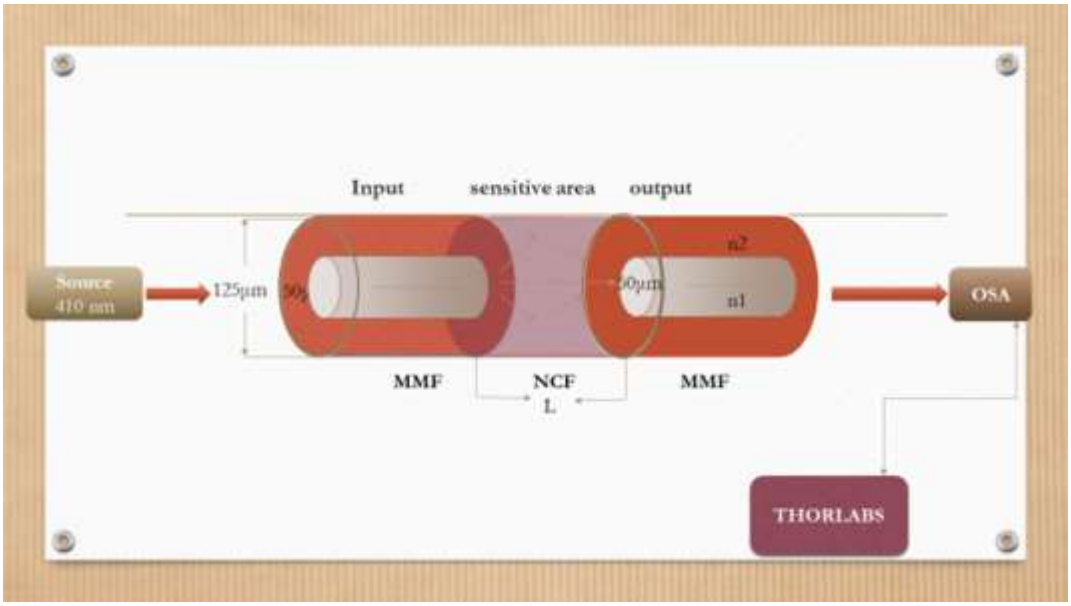

Figure(1): Fiber optic biosensor based on linked multimode no core multimode structure.

Figure(2): Fusion splicer S-16

The two ends of fiber were connected with an adapter device .An adapter is used for connecting the optical fiber with the laser from one side and the spectrum analyzer (OSA) from the other side.The source (410nm) was measured alone, then the turbidity of the samples was measured to 0.5 by a MacFarland standard to measure the intensity of *H.pylori* bacteria which detection by the biosensor.

Results and discussion

In this study, samples were taken from 10,five of it were positive.The isolation rate of *H.pylori* using Columbia blood agar was most of it positively as shown in figure (4) and it is also positive for urease as shown in figure (5) in addition to catalase, and oxidase-positive results as shown in figure (6) difference between each peak is the number of *H.pylori* cells in each drop.

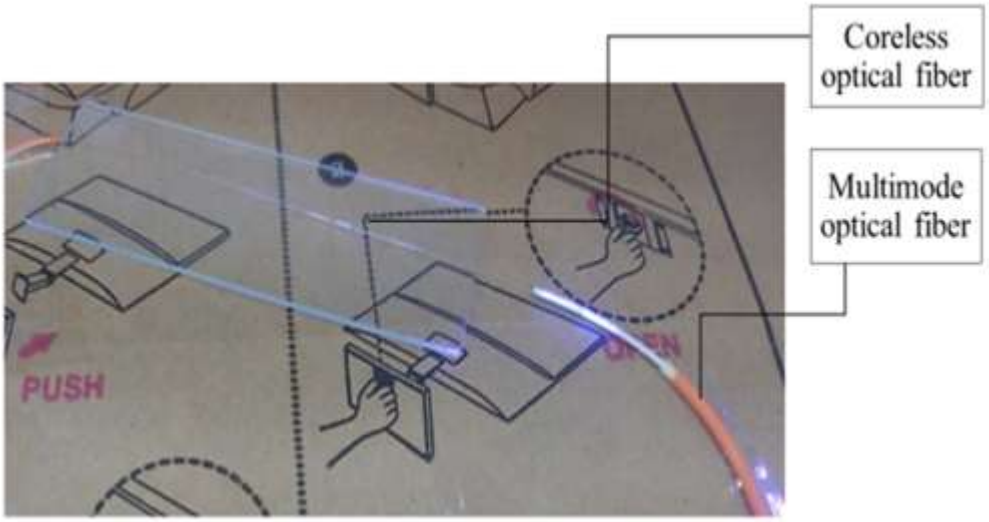

Figure (3) The Optical Biosensor Setup

Figure(4): h.pylori on selective Columbia blood agar culture

Figure(5) urease test agar

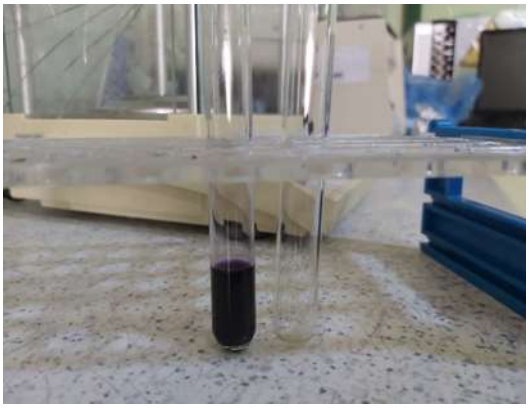

Figure(6): catalase, and oxidase test

Bacterial contamination of the medium by fungi and bacteria was common. The contaminating bacteria were Pseudomonas aeruginosa, the genus Proteus. Klebsiella can cause

contaminated biopsy forceps and contamination during collection, transport, and preparation of derailed sheep blood added to Columbia blood agar so the growth rate of H.pylori on this medium was slow and difficult to isolate so it was used the biosensor technique sensitive that produced rapid results for the determination of *Helicobacter pylori*. Flavin chemicals, together with porphyrins, as endogenous photosensitizers responsible for H. pylori photoinactivation have been identified for the first time in our spectroscopical and mass analytical analyses of bacterial extracts. Porphyrins, PPIX, CPI, and III, as well as flavin-type compounds like riboflavin, are among the endogenous photosensitizers responsible for bacterial photokilling.)Which absorb at 410 nm. after activating the samples for 24h, Broth media droplets (50 μm) are added to the coreless section(sensitive area).Detection is done by passing laser light from the source through the Multi-Mode area and passing it through the first splicing area. part of the light passing without reflection, while the other part is reflected from the splicing area to the coreless (sensitive area) to be absorbed by bacteria and reflected again to the second splicing area, which It collects light to pass through the multimodal region to the OSA (that inline Mach-Zhender interferometer)as shown in the figure(7)

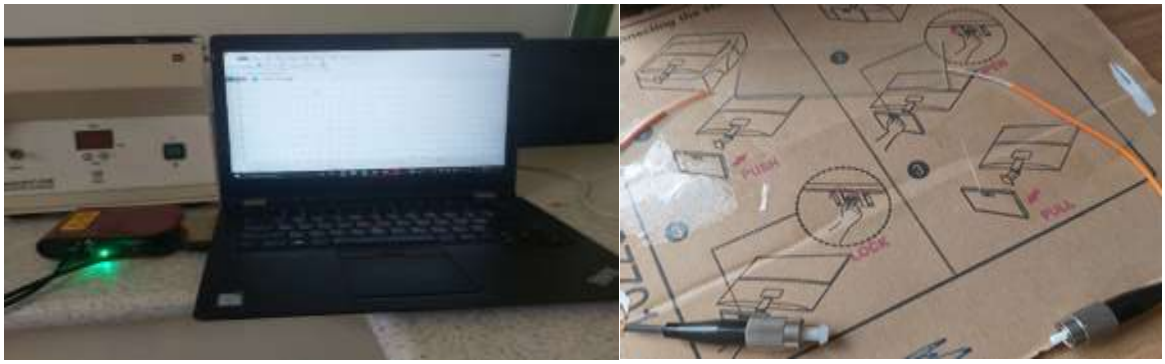

Figure(7): Biosensor setup in the lab

The Thorlab was showed a relationship between intensity and wavelength.Intensity is inversely proportional to the number of bacteria cells in the medea.The less the number of *H.pylori* bacteria the greater the intensity(Huang *et al.*, 2017) So Helicobacter pylori are measured as is shown in figures (8, 9, 10, 11, 12, 13). The time of the examination did not exceed half an hour, because *Helicobacter pylori* is an anaerobic bacteria, and thus the bio-sensor provided a safe, easy and fast method suitable with the conditions and sensitivity of bacteria. The results are comparable to previously reported multimodal interferometers based on more complex query schemes, and the MCM biosensor is a viable alternative for sensitive and easy measurements of H.pylori bacterial samples. Table (1) discuss the results where the

Table(1): Show results of culture, mean, variance, standard deviators, and range of wavelength in (nm).

samples	culture	mean	variance	Standard deviators	Range(nm)air
1	+	0.3361	0.0274	0.1657	406.2-406.7 nm
2	+	0.5124	0.07255	0.2694	406.6-406.7 nm
3	+	0.347	0.0012	0.0351	406.2-406.7 nm
4	+	0.4146	0.03393	0.1842	406.2-406.7 nm
5	+	0.2756	0.0027	0.05258	406.0-406.5 nm
source		0.0993	0.0004433	0.02119	405.6-406.07nm

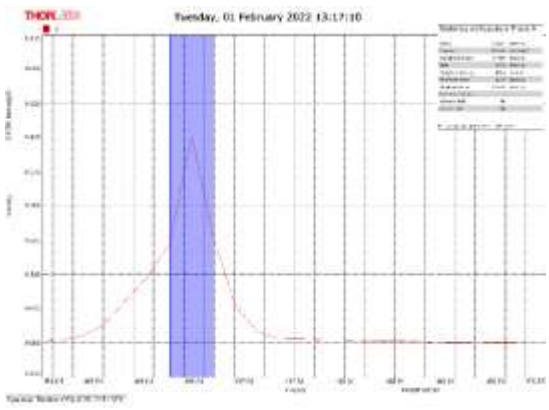

Figure(8): the peak of sample no.1

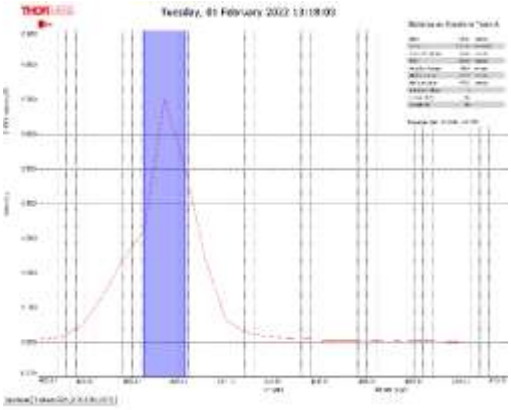

Figure(9): the peak of sample no.2

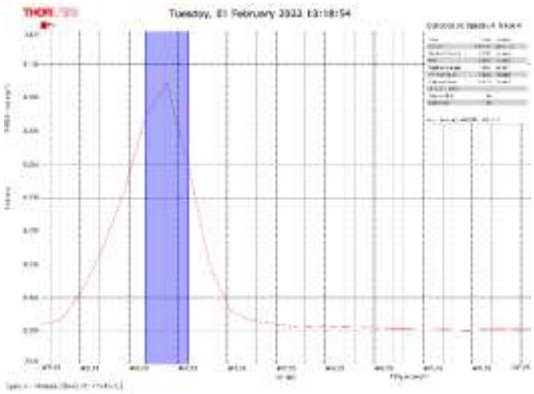

Figure(10): the peak of sample no.3

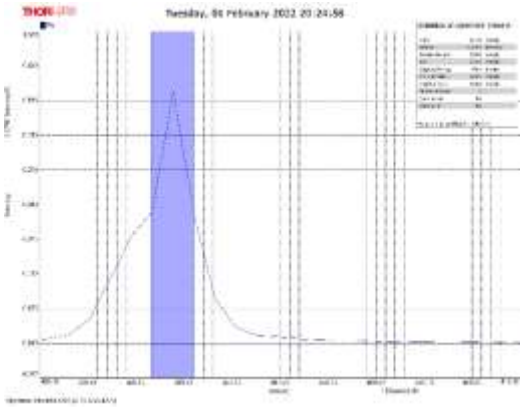

Figure(11): the peak of sample no.4

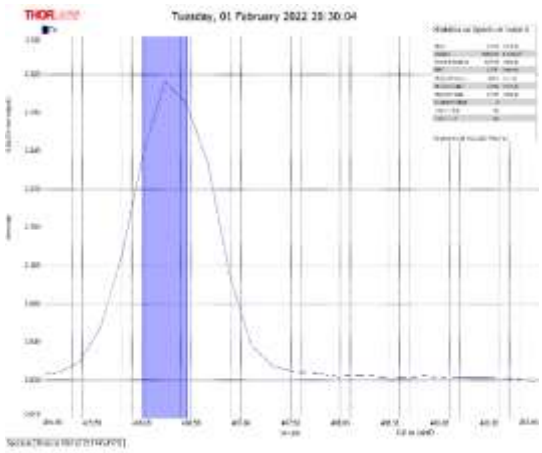

Figure(12): the peak of sample no.5

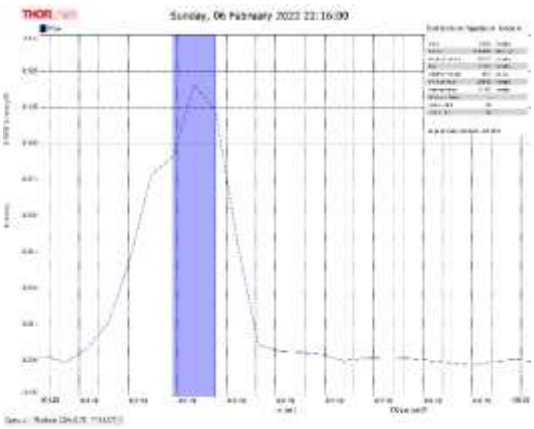

Figure(13): the peak of source

Conclusions

The isolation rate of *H. pylori* using Columbia blood agar was most of it positive. Bacterial contamination of the medium by fungi and bacteria was common. Our spectroscopical and mass analysis studies of bacterial extracts indicate for the first time flavin compounds, along with porphyrins as endogenous photosensitizers responsible for *H.Pylori* photoinactivation. The MCM biosensor was built based on the inline Mach-Zehnder interference is a viable alternative and rapid for sensitive and easy measurements of *H.pylori* bacterial samples. The results are comparable to previously reported multimodal interferometers based on more complex query schemes.All samples had a sensitivity ranging between 406.0 - 406.7 nm. Multimode-Coreless-Multimode optical Biosensor: is a rapid and sensitive method for the detection of *H.pylori* bacteria. (Statically) not all *H.pylori* isolates harbor the *Ure A* gene encoded for urease production

References

Bobrinetskiy, I. *et al.* (2021) "Advances in nanomaterials-based electrochemical biosensors for foodborne pathogen detection," *Nanomaterials*, 11(10), pp. 1–26. doi: 10.3390/nano11102700.

Cheng Y, F. (2017) "Biosensors for Bacterial Detection," *International Journal of Biosensors & Bioelectronics*, 2(6), pp. 197–199. doi: 10.15406/ijbsbe.2017.02.00048.

Huang, X. *et al.* (2017) "An in-line Mach-Zehnder Interferometer Using Thin-core Fiber for Ammonia Gas Sensing With High Sensitivity," *Nature Publishing Group*, (April), pp. 1–8. doi: 10.1038/srep44994.

Koyun, A., Ahlatcolu, E. and Koca, Y. (2012) "Biosensors and Their Principles," *A Roadmap of Biomedical Engineers and Milestones*. doi: 10.5772/48824.

Monošík, R., Streďanský, M. and Šturdík, E. (2012) "Biosensors - classification, characterization and new trends," *Acta Chimica Slovaca*, 5(1), pp. 109–120. doi: 10.2478/v10188-012-0017-z.

Pandey, A. *et al.* (2017) "Graphene-interfaced electrical biosensor for label-free and sensitive detection of foodborne pathogenic E. coli O157:H7," *Biosensors and Bioelectronics*, 91(December 2016), pp. 225–231. doi: 10.1016/j.bios.2016.12.041.

Ra, M. *et al.* (2012) "Biomedical applications of nanobiosensors: The state-of-the-art," *Journal of the Brazilian Chemical Society*, 23(1), pp. 14–24. doi: 10.1590/s0103-50532012000100004.

Usman, F. *et al.* (2019) "A Review of Biosensors for Non-Invasive Diabetes Monitoring and Screening in Human Exhaled Breath," *IEEE Access*, 7(December), pp. 5963–5974. doi: 10.1109/ACCESS.2018.2887066.

Yamaoka, Y. and Graham, D. Y. (2013) "Helicobacter pylori," *Brenner's Encyclopedia of Genetics: Second Edition*, pp. 409–411. doi: 10.1016/B978-0-12-374984-0.00688-4.

تقنية الاستشعار الحيوي للكشف عن بكتيريا الملوية البوابية

اسراء مطلك الصقري، أ.م.د.ليلى محمد العامري

معهد الليزر للدراسات العليا ، جامعة بغداد ، بغداد ، العراق

الخلاصه

الملوية البوابية هي سبب مهم لمرض الاثني عشر المعدية ، بما في ذلك قرحة المعدة ، والأنسجة اللمفاوية المرتبطة بالغشاء المخاطي ((MALT، وسرطان المعدة. أصبحت المستشعرات الحيوية أكثر التخصصات التي تمت دراستها على نطاق واسع لأن المستشعرات الحيوية السهلة والسريعة ومنخفضة التكلفة والحساسة للغاية والانتقائية للغاية تساهم في التقدم في أدوية الجيل التالي مثل الطب الفردي والكشف عن نقاط الرعاية فائقة الحساسية لعلامات الأمراض. شارك في هذا البحث خمسة من عشرة مرضى مصابين بالبكتيريا الحلزونية البوابية تتراوح أعمارهم بين 15 و 85 عامًا. من [التهاب المعدة ، والتهاب الاثني عشر ، وقرحة الاثني عشر ((DU، والقرحة الهضمية [(PU)تم التعرف على مستعمرات الملوية البوابية المشتبه بها من خلال وجود اليورياز ، والكتلاز ، ونشاط أوكسيديز ، و .PCRتم إصلاح جميع المعلمات: طاقة الليزر: 40 ميغاواط ، حجم القطرات: 25 ميكرومتر ، التعكر: 0.5. ، ألياف بصرية متعددة الأوضاع ، وألياف ضوئية عديمة النواة لبناء ألياف بصرية مستشعر حيوي ضوئي (متعدد الأوضاع - عديمة النواة - متعدد الأوضاع) استنادًا إلى مقياس تداخل Mach-Zehnder مضمن. جميع العينات لديها حساسية. المستشعر البيولوجي البصري متعدد الأوضاع - عديم النواة - متعدد الأوضاع: طريقة سريعة وحساسة للكشف عن بكتيريا الملوية البوابية.

Iraqi J. Laser, issue 2, vol., 21, pp. 9-15 (2022)

IRAQI JOURNAL OF LASER

Study the Effect of Nano Aluminum Oxide Coating on PMMA as Thermal Insulator

Dawood Obied Altiafy *, Hussien Ali Jawad, Noor Taha Ismaeel

Corresponding author*: ***dawood@ilps.uobaghdad.edu.iq*
hussein@ilps.uobaghdad.edu.iq
noor.t@ilps.uobaghdad.edu.iq

Institute of Laser for Postgraduate Studies, University of Baghdad, Baghdad, Iraq

(Received 14/5/2022; accepted 1/12/2022)

Abstract: In the present work, the heat transfer of Nano Aluminum Oxide -NAO- has been studied practically to define the appropriate insulation conditions. This study focuses on finding of the amount of heat transfer through a glass substrate that is coated with nanoalumina doped on PMMA matrix. The optical and thermal properties were systematically investigated. The density of heat flow rate, was calculated in the range values (240-260) W/m2 while the optimum values confine between (250-260) W/m2 at temp. (25-35)C^{o}. The results showed that the thermal insulation of the sample was significantly enhanced at temp. (30-50)C^{o}. The simulated net heat transfer through window decreased linearly with increase of both of coating thickness concentration. Furthermore, the overall transmittance in the visible region and reflectance in infrared and ultraviolent regions decrease with increasing of weight content of the coated film.
Keywords: ??????

1. Introduction

The development of solar energy production is one of the most efficient ways to provide for the world's needs [1]. On the other hand, thermal insulators should be introduced for protection against the increasing temp. that leads to increase heat transfer. The Thermal insulators are those materials that prevent or reduce various forms of heat transfer (conduction, convection and radiation). Insulator resists the heat transfer from out to in or in opposite direction whether the environment temperature is high or low. The thermal insulating materials have increased during the last decades as a result of increasing in environmental conditions. One of the problems is how to stop the heat to transfer through glass windows. One of the factors causing temperature rise is the heat transmitted the process of heat conduction and radiation. The heat gain or loss can be minimized if good insulating material is used.

Metal oxide nanoparticles have good stability, low poisonousness, and selectivity linked with organic substances [1-4]. This higher quality provides much better thermo-physical properties. Nanoscale Aluminum Oxides are considered ideal due to their high thermal conductivity, insulation, and low thermal expansion coefficient. Nano Aluminum Oxide is considered as a form of efficient thermal barrier between the glass substrate and air. This kind of spray coating is very simple, but its application was efficient for improvement of surface quality [2].

When light strikes the surface of a solid target, part of it will be absorbed, which means its energy is converted to heat. Another part of the incident light is reflected, and another amount could be transmitted. The absorbed heat is gained indoors by the target through conduction while energy is lost outdoor through convection and radiation. The heat gain passing through glass will inversely proportion with the insulation of the film coated.

There are many literature surveys available which shows the relation between the thermal conductivity and heat transfer characteristic with concentration of nano particles.

Omar O., Mounir K., Mohamed L., studied the application of nanofluids in solar collectors, they examined the thermophysical properties of nanofluids [1].

Kusammanavar B. et al., summarize how increased concentration of nano particles increases the thermal conductivity and heat transfer rate.[3]

M. S. Kamel et al., were experimentally measured, the trmal conductivity of alumina, ceria, and their hybrid with ratio (50:50) by volume-based deionized water nanofluids their results have showed good agreement within the accuracy of the thermal conductivity tester [8].

The aim of the present research is to improve the thermal insulation of car windscreen to reduce heat transfer by studying the thermal properties of PMMA coated with nano Al_2O_3. This film could be added inside window to enhance thermal insulation.

2. Materials and Methods

Substrate Preparation

The preparation of PMMA is obtained by dissolving 0.7 g of PMMA in 10 ml acetone to get the homogenous solution. The magnetic heater stirrer was used as a source of heating and to mix the solution. The degree of heat must be less than the degree of its glass transition temperature (Tg 105C^o). Substrates (PMMA) were prepared by spraying of alumina nanoparticles along PMMA sheets. For each spraying line it was considered as one layer.

As the diagram below:

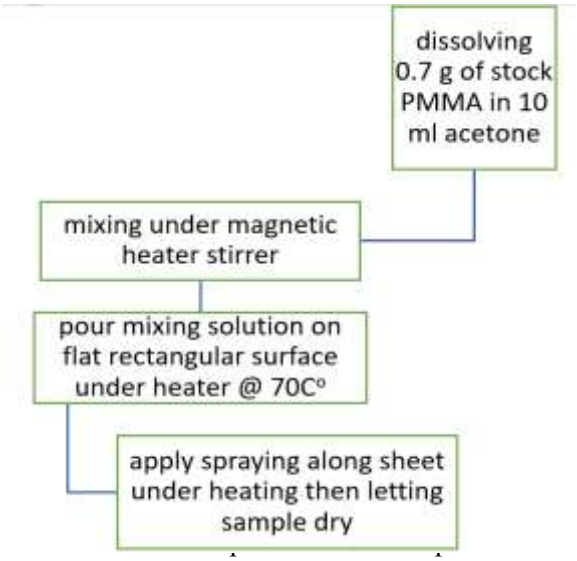

USA Company with the following specification:

Item	Nano-AL_2O_3 specification
Manufacturer	USA
Appearance	White
Assay	99.99%
PH value	7.5
Grain size	30-60nm
Bulk density%	0.43

The glass wall first cleaned with distilled water followed by rinsing in chromic acid (for 24 hours) which formed the basis for the thin film growth. Then the glass box was washed in deionized water. The experimental apparatus primarily consisted of as shown in Figure (1).

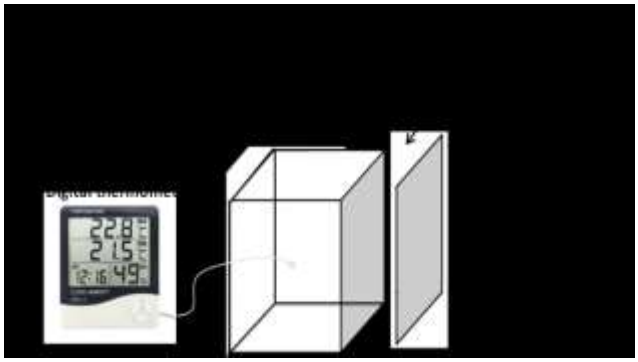

Figure (1): Glass box chamber with four sided coated as a series of coating layers.

The glass chamber with the size (15 x10x10 cm and 0.5 cm glass thickness) was prepared. As

shown in Figure 3, Two faces of the glass box were coated with -NAO- in multi-layer staring from one to three layers, while other faces cleaned and washed to ensure the whole solar radiation passes through and to make comparison. The PMMA sheets were heated before applying spray to ensue uniform distribution of coating as well as the sheet was angled at 45^o to remove any extra coating while spraying.

The box was exposed to the solar radiation in the mid-afternoon for two hours, where the temp. was 40C^o to ensure the thermal absorption of the box with its wall. Moreover, the sun radiation was incident normally on the box. The measurement of thermal radiation was done via a digital thermometer, which is placed inside the box chamber. Firstly, the heat gain was recorded as zero-reading (reference reading) from non-coated walls of the chamber. The other readings were collected via the coated walls at different exposed solar radiation time.

3. Spectroscopic Measurements

T60UV-Visble Spectrophotometer and spectrofluorometer for measuring the transmission and fluorescence respectively (PG-instruments company). The UV-visible spectrophotometer, Wavelength range 190 nm – 1100 nm, Light source is Tungsten lamp power of 10W and the Detector is Silicon photodiode. While the fluorescence spectrophotometer specifications are Spectral Range from 200 to 700 nm and Scanning rate 200, 400 & 600 nm/min. The Light source 150 watt Xenon arc lamp and the detector is high sensitivity photo multiplier tube (PMT)

4. Thickness Measurement

The Michelson interferometer instrument (from lambda scientific company) was used to measure the thickness of thin film**.** In the Michelson interferometer the collimated beam of light is divided into two parts by partial reflection, which can be used to measure the thickness of the coated thin film. Figure (2) shows the precision interferometer instrument with specifications: Flatness of Beam Splitter & Compensator Plate 0.05. Minimum Travel Reading is 0.00025 mm. Fabry-Perot Mirrors 30 mm (dia), R=95% and Wavelength Measurement Accuracy. The source is He-Ne Laser Output 0.7 ~ 1 mW at 632.8 nm and Overall Dimension 350 mm×350 mm×245 mm.

Figure (2): precision interferometer

The thickness of layer was measured by Michelson interferometer method. The fringes pattern is shown in Figure (3)

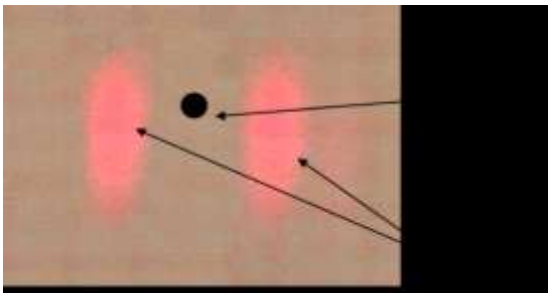

Fig. (3) : The interference fringes pattern of nanoalumina-PMMA thin film

The number of fringes (N) were counted through a fixed point on the screen, Using the following formula to determine the thickness [7]:

$$n = \frac{n_o^2\ d\ sin^2\theta}{2n_o d(1-\cos\theta) - N\lambda} \qquad \text{Eq. (1)}$$

n: the refractive index of slice.
n_o: the refractive index of air (1),
d: the thickness of thin film.
θ: the angle of inclination.
N: the number of fringes

The thickness of layers was calculated as (1µm for one coated layer, 1.5µm for two coated layers and 1.8 µm for three coated layers)

It is found that the average thickness of the deposited thin films affects directly on the amount of the substrate temperatures, which in turn limits the heat transfer to the interior system [3].

5. Results and Discussion

UV-vis spectrum

The optical absorption of the ceramic nanoparticles was analyzed using UV-VIS spectrophotometer T60. Figure (4) shows the absorption spectrum of the nanoalumina-PMMA.

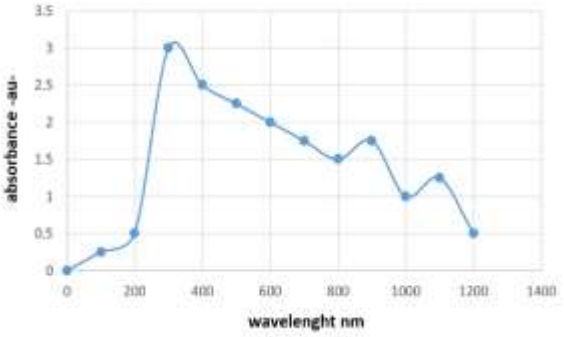

Figure (4): The absorption spectrum of nano-alumina-PMMA.

The optical absorption of the -NAO- shows a variable behavior of the transmission as a function of the incident wavelength. The visible region shows gradual absorption from higher values at 400nm to lower values at 700nm to 800nm.

The absorption peak of thin film at 300nm. This is because of the photoexcitation of electrons from the valence band to the conduction band, the spectrum has a good agreement with [2]. At higher wavelengths, the absorption is limited to lower values. The main feature of the spectrum is that the visible spectrum can be transmitted through the coated glass wall.

FTIR spectrum

FTIR Characterizations of the Transition Al_2O_3. FTIR spectra are reported in Figure (5). The spectrum in the range 400–1000 cm^{-1} represents a crystallized structure characterized by a broadband with a thin peak appear at 457, 488 604 and 641 cm^{-1}. This signature is that of the Al_2O_3 (the broad extending band in the range 400–700 cm^{-1} indicating the presence of a better crystallized phase of nanoparticles in this spectrum [2]. Thus, the IR spectroscopy in the range 400–1000 cm^{-1} can be used as a fast and easy tool to identify the Al_2O_3 phases.

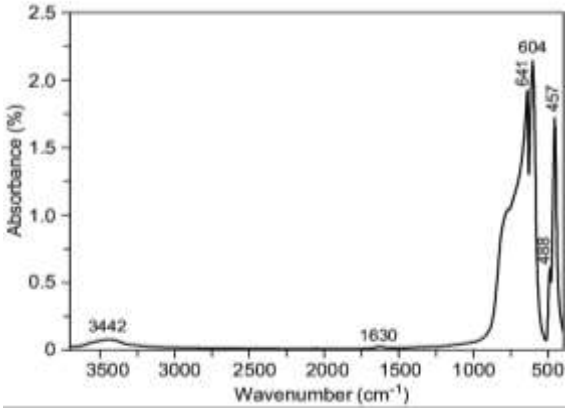

Figure (5): The FTIR spectrum of nano-alumina-PMMA.

Heat transfer profile

Heat transfer processes of the glass window coated with -NAO- can be quantified in terms of appropriate rate equations. These equations may be used to compute the amount of energy being transferred per unit time. For heat conduction, the rate equation is known as **Fourier's law**. For the one-dimensional plane wall shown in Figure (6), having a temperature distribution T(x), the rate equation is expressed as[4]:

$$\frac{dq}{dt} = -\lambda A \cdot \frac{dT}{dx} \qquad \text{Eq. (2)}$$

Where

q = quantity of heat in time (t)

A = area perpendicular to the flow, (for on-dimensional heat flow A = 1 m2)

λ (Lambda value) = coefficient of thermal conductivity = 38.5 W/m.K [4]

(the negative sign because T2 < T1).

dT/dx = the temperature gradient.

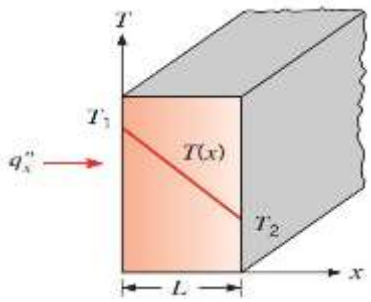

Figure (6): One-dimensional heat transfer by conduction (diffusion of energy)

For steady state one-dimensional heat flow, the conductivity equation can be written as [4]:

$$q = -\lambda . \left(\frac{T2 - T1}{L}\right) = -\frac{\lambda}{L}(T2 - T1) = -K\,\Delta T$$

Where q = density of heat flow rate, W/m^2
K = thermal conductivity $[W.m^{-1}.\ k^{-1}]$
T1 and T2 = temperature at either end of the flow path. Table (1) shows the calculated variation of density heat flow according to coated layers thickness at different irradiation energy coming from solar system.

Table (1): numerical values of density heat flow at different coating layers.

	Layer 1			Layer 2			Layer 3		
no.	temp. in C^o	output	density of heat flow rate -q-	temp. in C^o	output	density of heat flow rate -q-	temp. in C^o	output	density of heat flow rate -q-
1	25	23	260.8	25	18	256.	25	11	249.2
2	30	25	257.9	30	22	255.0	30	13	246.4
3	35	32	259.8	35	29	256.9	35	15	243.5
4	40	38	260.8	40	33	256.0	40	18	241.5
5	45	44	261.8	45	37	255.0	45	30	248.3
6	50	49	261.8	50	45	257.9	50	38	251.2
7	55	55	262.7	55	50	257.9	55	45	253.1
8	60	60	262.7	60	58	260.8	60	53	256.0

Figure (7) represents the directly relation of transmitted heat through coated window. The main feature of the curve is that increasing the thickness of thin coated film should lower the transmitted heat energy. While Figure (8) represents the behavior of heat flow density which take a variable value according to the environment solar irradiation, the minimum density profile can be observed at $40C^o$ which define the minimum heat transfer at a specific thin coating ratio.

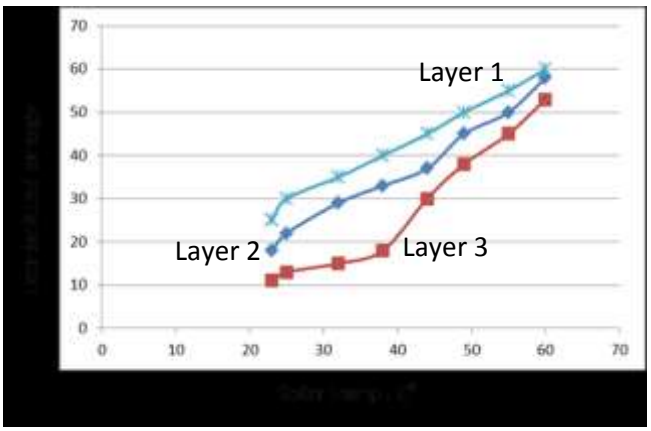

Figure (7): the relation between the irradiation solar temperature and the transmitted heat through coated window

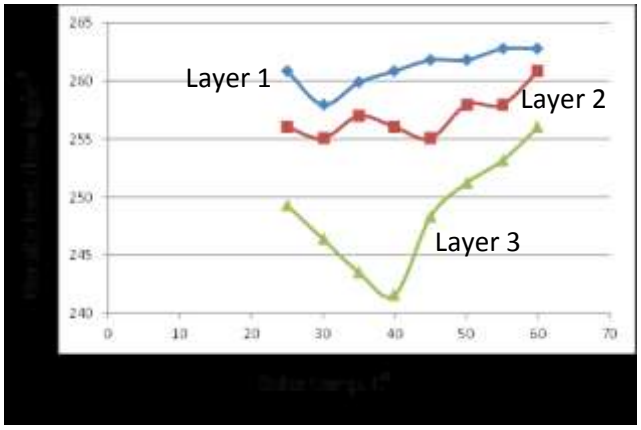

Figure (8): the density of heat flow as a function to the irradiation solar energy

The inner surface of cellular thin film nanoparticles layer 3 works as a heat mirror and reflect the 30-50% of heat radiation, this can be defined by division of transmitted temp. with input radiation then deduct from unity. Thermal conductivities have been measured with longitudinal heat flow methods where the experimental arrangement was designed to accommodate heat flow in only the axial direction, temperatures are varied, and radial heat loss is prevented or minimized. On the other hand, an increase in the thickness of coated film will decrease the heat transfer rate and this is observed if the area is maintained constant. In other words, the rate of heat transfer is directly proportional to mass flow rate. When increase the flow rate, an increase in the rate of heat transfer was observed.

Thermal conductivity of -NAO-

Nowadays, -NAO- consider as a modified method used to enhance thermal performance in different applications. Figure (9) shows the behavior of thermal conductivity against temperature gradient.

It can be seen form the figure that there is slightly decrease in thermal conductivity at temp. range (25-40) C^o and this drop express the enhancement of thermal barrier of the film which can be considered as positive results for the minimum purpose of this study, however, this can be more clearly by analyzing the thermal conductivity from equation (1), which showed that as the temp. differences (T2-T1) increases the thermal conductivity will decrease and vis versa. The large amount of ΔT reflects the minimum heat transfer through -NAO- barrier.

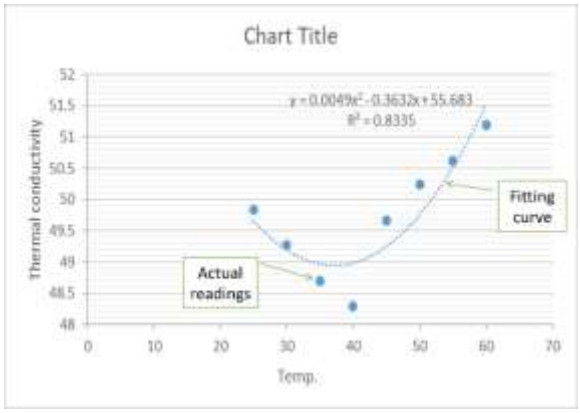

Figure (9): thermal conductivity versus temperature gradient.

On the other hand, the increasing of suppling temperature (more than $50C^o$) shows the increase of thermal conductivities. This is because both adding nanoparticles and higher temperatures lead to increased interaction between nanoparticles and a base polymer, resulting in increasing effective thermal conductivity. Enhancement in thermal conductivities plays a major role in improving the thermal performance. It was found that the values of thermal conductivities in the present study agree well with those from the previous study [8, 9, and 10].

6. Conclusion

This research deals with the development of film (PMMA doped -NAO-) for solar heat barrier depending on spectral selectivity and photothermal effect, related to heat transfer. The key that limits the heat flow through windows is the thermal insulation. In particular, the film showed its activity as thermal insulation via the insulation effect of the nanostructured at specific temp. one of disadvantages is the high cost of this product especially for large area design, so that the cost should be considered when designing windscreens.

References

[1] O. Ouabouch, M. Kriraa, M. Lamsaadi, "Stability, thermophysical properties of nanofluids, and applications in solar collectors" AIMS Materials Science, 8(4): 659–684, (2021).

[2] M. I. Kandil, H. S. Jahin, et al., "Synthesis and characterization of γ- Al_2O_3 and α-Al_2O_3 nanoparticles using a facile, inexpensive auto-combustion approach" Egypt. J. Chem. Vol. 64, No. 5 pp. 2509 - 2515 (2021).

[3] K. Basavaraj, K Elangovan, et la., "Effect of Concentration of Al_2O_3 Nano Particles in Base Fluid on Thermal and Flow Properties to Enhance the Heat Transfer Rate" International Journal of Engineering Research & Technology (IJERT), Vol. 10 Issue 02, (2021).

[4] Y. Sharma, N. Yadav, "Enhancement in Heat Exchange Process in a Shell and Tube Heat Exchanger using Nano Particles" International Journal of Engineering and Advanced Technology (IJEAT), Vol.9 Issue-3, (2020).

[5] Analytical Instruments for Science, PG instruments, Alma Park, Wibtoft Leicestershire, Le17 5bh, United Kingdom, https://www.pginstruments.com

[6] LEOI-22 Precision Interferometer, Lambda Scientific Systems, Inc. 16300 SW 137th Ave, Unit 132 Miami, FL 33177, USA, https://lambdasys.com/

[7] R. Phillip Scott, "Measuring the Thickness of Thin Metal Films" A senior thesis, Brigham Young University – Idaho, (2012).

[8] M. S. Kamel, O. Al-Oran, F. Lezsovits, "Thermal Conductivity of Al_2O_3 and CeO_2 Nanoparticles and Their Hybrid Based Water Nanofluids: An Experimental Study" Periodica Polytechnica Chemical Engineering, 65(1), pp.50–60, (2021).

[9] M. Kong, and S. Lee, "Performance evaluation of Al2O3 nanofluid as an enhanced heat transfer fluid" Advances in Mechanical Engineering, Vol. 12(8) 1–13, (2020).

[10] S. Porgar and N. Rahmanian, "Investigation of Effect of Aluminium Oxide Nanoparticles on the Thermal Properties of Water-Based Fluids in a Double Tube Heat Exchanger" Biointerface Research in Applied Chemistry, Vol. 12, Issue 2, 2618 – 2628, (2022).

دراسة تأثير جزيئات أكسيد الألومنيوم النانوية على PMMA كحاجز حراري

داود عبيد الطيفي حسين علي جواد نور طه اسماعيل

معهد الليزر للدراسات العليا ، جامعة بغداد ، بغداد ، العراق

الخلاصة: في هذا البحث تم تقديم مقدار انتقال الحرارة داخل النافذة الزجاجية. توفر مواد PMMA المطلية بالنانو ألومينا في النوافذ مستويات إضاءة كافية في المناطق الداخلية للمباني وكذلك في الزجاج الأمامي للسيارة الذي ينفذ منه الجزء المرئي من الإشعاع الشمسي. الجزء الآخر من الإشعاع الشمسي في منطقة الأشعة تحت الحمراء التي تدخل من خلال النوافذ يتسبب في زيادة درجة الحرارة الداخلية. ومن ثم تعد هندسة النوافذ الزجاجية مكونًا رئيسيًا في تصميم وتحليل المشكلات مثل متطلبات الطاقة وتقييم أحمال التدفئة والتبريد والراحة الحرارية في العديد من التطبيقات. تركز هذه الدراسة على دراسة سلوك انتقال الحرارة بالإشعاع من خلال الزجاج المطلي بألومينا نانوية المترسبة على ركيزة PMMA. أجريت الدراسة لتطوير الطلاء النانوي الوظيفي للنوافذ الزجاجية للظروف الإقليمية في العراق. تم طلاء طبقات متعددة على شكل غشاء رقيق مع خصائصها الضوئية والحرارية تم فحصها بشكل منهجي. تم حساب معامل اكتساب الحرارة الشمسية وصافي انتقال الحرارة من خلال النافذة. أظهرت النتائج أن العزل الحراري لتأثير الزجاج لسمك الطلاء ومستوى المنشطات كان معنوياً. انخفض مستوى انتقال الحرارة عبر النافذة خطيًا مع زيادة تركيز سماكة الطلاء. علاوة على ذلك ، فإن النفاذية الكلية في المنطقة المرئية والانعكاس في مناطق الأشعة تحت الحمراء والأشعة فوق البنفسجية تتناقص مع زيادة محتوى كمية الطبقة المطلية.

Iraqi J. Laser, issue 2, vol., 21, pp. 16-24 (2022)

IRAQI JOURNAL OF LASER

Study the Effect of Gold Film Thickness on the Sensitivity of the U Shape Fiber Sensor by the Occurrence of LSPR Phenomenon

Saffana Z. Maseer[1,*], Bushra R. Mahdi[2]

**Corresponding author: saffana.zeiab1202a@ilps.uobaghdad.edu.iq*.

1. Institute of Laser for Postgraduate Studies, University of Baghdad, Iraq, Baghdad, Iraq.
2. Ministry of Science and Technology, Materials Research Department, Laser Center, Iraq, Baghdad.

(Received 4/7/2022; accepted 19/9/2022)

Abstract: In this paper, a U-shaped probe with a curvature diameter of half a centimeter was implemented using plastic optical fibers. A layer of the outer shell of the fibers was removed by polishing to a D-section. The sensor was tested by immersing it in a sodium chloride solution with variable refractive index depending on solution concentrations ranging from 1.333 to 1.363. In this design, the sensor experienced a decrease in its intensity as the concentration of the solution increased. The next step The sensor was coated with a thin layer of gold with a thickness of 20 nm, and the sensor was tested with the same solutions which resulted in a shift in wavelengths where the shift in wavelength was 5.37 nm and sensitivity 179 nm / RIU. To study the effect of the thickness of the film, it was coated with a second layer of gold to make the total thickness 30 nm. The results showed an improvement in the sensitivity with increasing the thickness of the coating, to become 466.66 nm / RIU and the wavelength shift was 14 nm.

Keywords: Plastic optical fiber, Gold NanoParticles, U Bend optical fiber, DC Plasma coating.

1. Introduction

Numerous fiber-optic sensing devices have been studied and created during the last two decades. [1]. Refractive index (RI) sensors, pH sensors, strain sensors, temperature sensors, curvature sensors, and humidity sensors are just a few of the sensing applications where optical fiber sensors have received significant attention [2],

Comparing fiber sensors to various traditional sensors, there are a number of benefits. Fiber sensors are small, light, have a high resolution, and good stability in addition to being immune to electromagnetic interference and able to withstand high temperatures and radiation[3].

Due to their ease of handling and economic efficiency, plastic optical fibers (POF) manufactured of polymethylmethacrylate (PMMA) are receiving more attention as a viable replacement to silica-based fiber optic sensors, because POF is so flexible, any required fiber probe design such as tapered, side-polished, U-bent, coiled, or any other may be easily achieved to get a strong evanescent field at the core-cladding interference[4]. Nanotechnology's most recent advancements have resulted in new breakthroughs for localized surface Plasmon

resonance (LSPR) fiber optical sensors. The shape, size, substance, and refractive index of the surrounding medium all influence the extinction range generated by the LSPR phenomenon[5][6]. Due to their excellent optical properties, gold nanoparticles (Au-NPs), a sensitive coating among nanosized metallic materials, are frequently used in optical sensing applications[7]. By coating the optical fiber with a controlled layer of gold nanoparticles, a reliable LSPR-based sensor may be produced[8]. Because the coating thickness must always be less than the evanescent wave's penetration depth, controlling the coating thickness on a nanoscale scale is a crucial quality for sensors based on the interaction of the evanescent field with the coating. The evanescent wave absorbance heavily depends on the analytic concentrations, assuming no other variables change[7]. When the probes coated with gold layer with thickness greater than the evanescent wave penetration depth would not lose light on the sensing region since the film transmittance was negligible such that practically all the light would be reflected and remain inside the fiber, so that the thicker the layer, the smaller the sensitivity[9].

Side-polished fiber, tapered fiber, hetero-core structured fiber, and U-shaped fiber are just a few of the fiber configurations that have been suggested to increase the sensitivity of fiber SPR. The U-shaped fiber SPR sensor has been proven to be more sensitive than the traditional straight fiber SPR sensor[10]. Part of the light from the core mode is coupled into the cladding and generates numerous sets of higher-order modes as it passes from the straight portion of the sensor fiber into the U-bent area, the guided light rays in the sensing region reflecting at angles closer to the critical angle and more optical power is decayed into the sensing medium this enhances the light matter interaction and the sensitivity increases[11]. Although U-shaped fiber sensors significantly increases sensitivity, in most cases structural modification techniques like tapering by polishing are employed to increase the sensitivity of optical fiber sensors. When the U-shaped outer curvature is removed by polishing, the evanescent field's power and penetration depth increase because when the outer curvature of the U-shaped POF is removed by polishing; the RI difference between the analytic and the inner curvature of fiber will decrease, leading to the increase of evanescent wave power, as well as its penetration depth. These structural modifications are used to improve the sensitivity better sensing performance is made possible by these structural changes[12]

The interplay of the evanescent field and the surface electron released by the Plasmon metal is the basis of the SPR sensor's working theory. An evanescent field is produced at the U-bent area of the fiber by a light wave that is propagating in its core[9]. When the evanescent field strikes the metallic surface, it produces a surface Plasmon wave (SPW), the SPW propagates along the metal-dielectric surface. If the frequency of the evanescent wave and surface Plasmon mode is matched, the excitation of surface Plasmon at metal/dielectric interface results in the transfer of energy from incident light to surface Plasmon when the energy of light photons perfectly matches the Plasmon's' energy level, which reduces the intensity of the output light[13]. Typically, the bend loss of U fiber sensor is comparable to the intensity modulation, which is easily impacted by the light source and the surrounding environment [14].

In this paper U shape plastic optical fiber sensor was built with 0.5 cm bending diameter and tested it with sodium chloride solutions with change in refractive index from 1.333 to 1.363 then coated it with 20 nm thickness of GNPs and retested with the same sodium solutions. Finally, coated the bare sensor with 30nm thickness of GNPs and tested it with same sodium solutions to study the effect of GNPs thickness on the sensitivity of the sensor.

2. Experiment Work:

Based on macro-bending fiber losses, U shape fiber sensor have been designed and constructed by using plastic optical fiber.

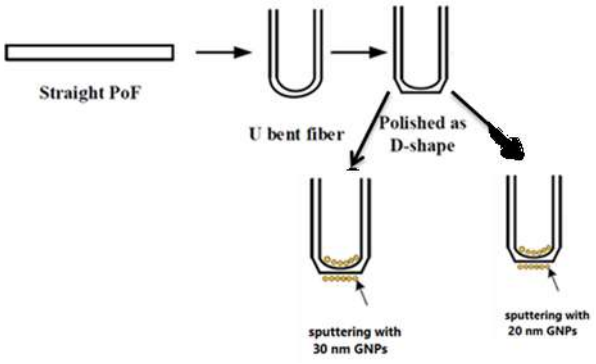

Figure1: steps of fabrication the sensor.

The steps of fabrication the sensor was shown in the figure 1.

Plastic optical fiber (POF) with 930 µm diameter was made of PMMA with refractive indices 1.49 and 1.41 for core and cladding respectively was used as shown in figure2.

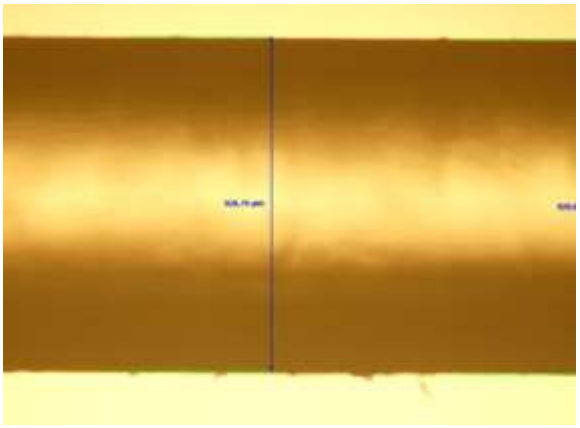

Figure2: straight Plastic Optical Fiber.

First, Straight Plastic optical fiber was bent in U shape handily with 0.5 cm bending diameter, the sensors were installed on a plastic graduated ruler and secured with thermal adhesive.

The U-bent POF head sensor is polished using grinding papers to make it resemble a D shape in cross section, as shown in figure3(a). To ensure polishing perfection, the POF must be rigidly fixed. The upper portion of POF was mostly removed to roughly construct the appropriate probe profile using a rough polishing paper with bigger particles. The roughness of the exposed area was then further reduced using fine emery paper with finer particles, as can be seen in Figure3b

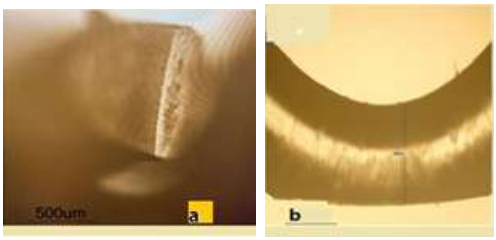

Figure 3: (a) Microscope image of the cross-section of the sensor tip from which the clad part has been removed and shown shape D. (b) Microscope image of polished POF, bent U-shape, fiber diameter after polishing 680 µm.

Finally, GNPs sputtered on the head sensor by using DC Plasma coating device. The deposition rate of the coating layer was 20nm/hour. DC scattered plasma technology, a vacuum coating process classified under Physical Vapor Deposition (PVD) systems and primarily used for the deposition of metal alloys, composite textiles and other materials. The gold target represents the cathode electrode (The gold target with a thickness of (1 mm) a diameter of (5 cm), and a purity of (99.9%)), followed by a Teflon ring to fix the samples to be coated, as shown in Figure 4a, and the parts of the complete system are shown in Figure 4b where sensors are mechanically fixed on the Teflon ring, which is stable in the vacuum chamber between the cathode (gold target) and the

anode, obtaining a coating film thickness of 20 nm.

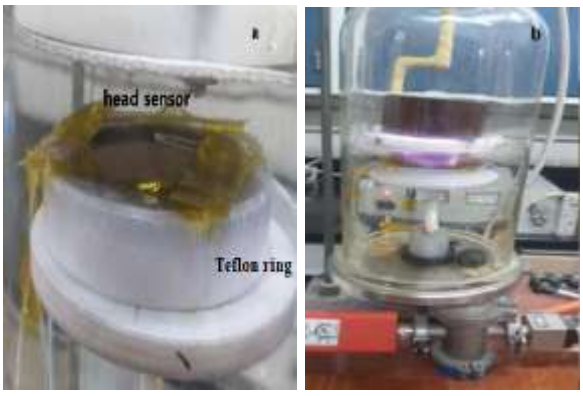

Figure 4: The demonstration system of DC Plasma coating device.

Figure 5 shows the sensor without coating in A and by coating a first layer with a thickness of 20 nm in(b) and a thickness of 30 nm in (c).

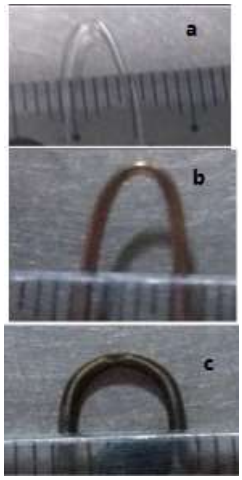

Figure5: (a) bare POF with 0.5cm bending diameter. (b) POF with0.5cm bending diameter was coated with 20nm thickness of GNPs. (c) POF with 0.5cm bending diameter was coated with 30nm thickness of GNPs.

The coated fibers were examined under an electron microscope to test the size of the gold particles, which are shown in Figure 6, with two different scales of the SEM microscope.

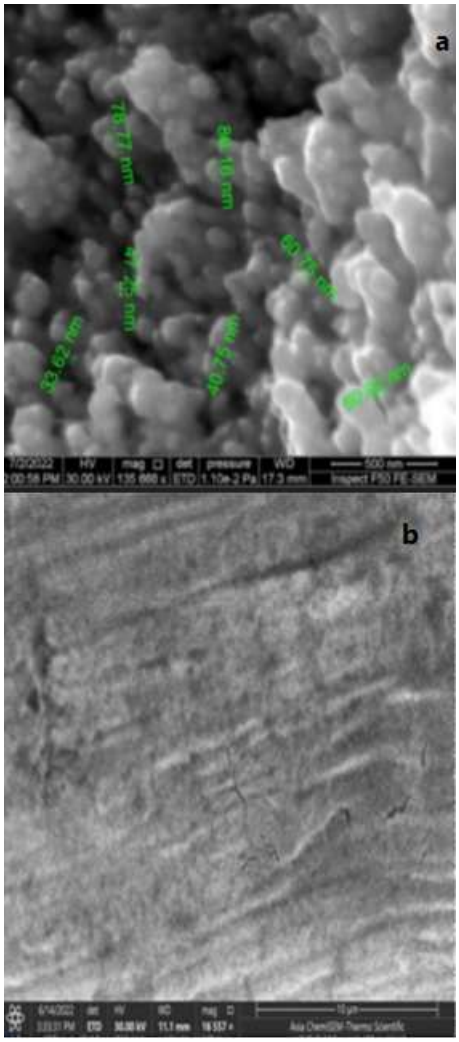

Figure 6: SEM (Scanning electron microscopy) image for GNPs in two scales (a) 500nm and (b) 10µm.

2.2 Experimental Setup:

In this experiment Semiconductor Laser with 650 nm and 5 mW was used as a source and Ocean 2000 was used as a spectrometer to record the laser beam transmitted on the computer as shown in figure 7.

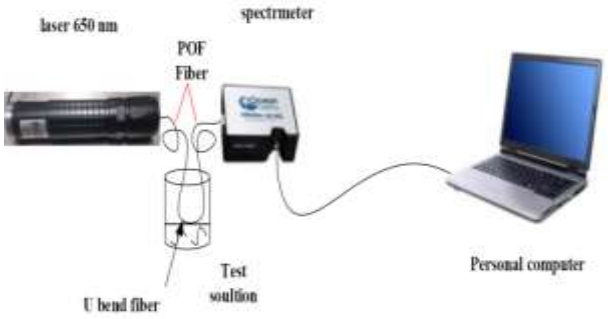

Figure 7: experimental setup.

2.3 Refractive Index solutions:

Sodium chloride solutions with different concentrations are used as samples with different RIs. NaCl solutions were prepared by taken different concentration values of the Salt powder dissolved in distal water at room temperature. Abbe refractometer measured the refractive index of the solutions with ranges (1.333-1.363).

Table 1: The refractive indices of the sodium chloride solutions.

RI	Abbreviation	Concentration
1.333	Distal water	0
1.339	C1	1mg/ ml
1.342	C2	2 mg/ml
1.350	C3	3 mg/ml
1.358	C4	4 mg/ml
1.363	C5	5 mg/ml

3. Result and Discussion:

Intensity counts (number of photons that the spectrometer was detected it) was recorded to characterize the NaCl solutions for U bent POF sensor with 0.5 cm bending diameter without coating.

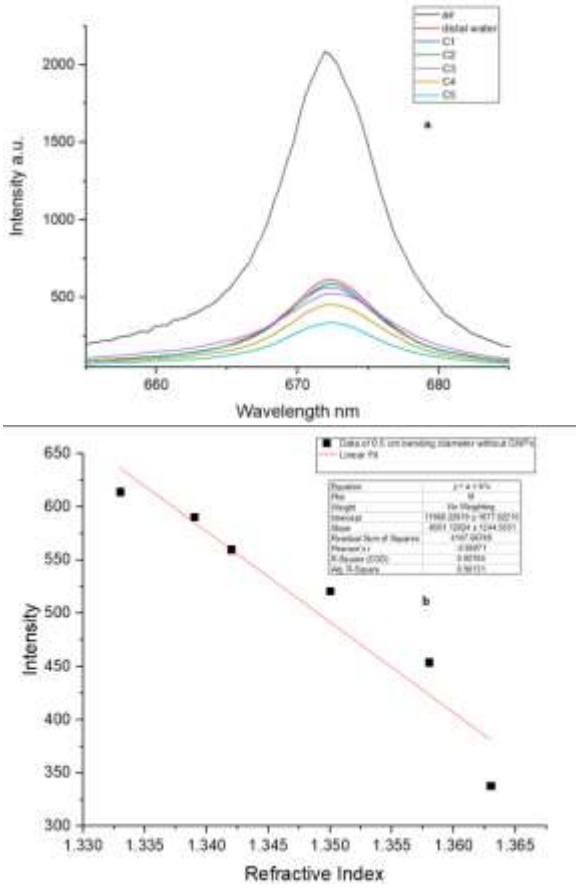

Figure 8: (a) Response of U shape bare POF sensor with 0.5 cm bending diameter to refractive index change. (b) Linear fit between Intensity and refractive index change.

It is noted in figure8 a that the intensity spectrum of sodium chloride solution with different concentrations and refractive indices ranges from 1.333 to 1.363, where there is no shift of wavelengths, but the intensity decreases with the increase in the concentration of the solutions this occurs because the increased concentration of chloride sodium solution increases absorption of light power by the solution resulting in decreasing in the intensity of light. The sensitivity of change the Intensity with refractive index change was -8501ΔI/RIU (ΔI/RIU change in intensity per refractive index change) for this sensor was calculated from the linear fit in figure 8(b).

Then LSPR wavelengths were recorded to characterize the NaCl solution for U shape POF sensor with 0.5 cm bending diameter with 20nm thickness of GNPs shown in figure9 and U bent POF with 30nm thickness of GNPs shown in figure 10.

It is evident from figure 9 (a) that as the concentration of NaCl solution increase the LSPR wavelength gradually move to longer wavelength (Δλ=5.37) with peak intensity decreasing. figure 9c show the linearity between the LSPR wavelength and the refractive index change the sensor response was showed to be linear with R^2= 0.96 and the sensitivity of LSPR wavelength with refractive index change was 179 nm /RIU.

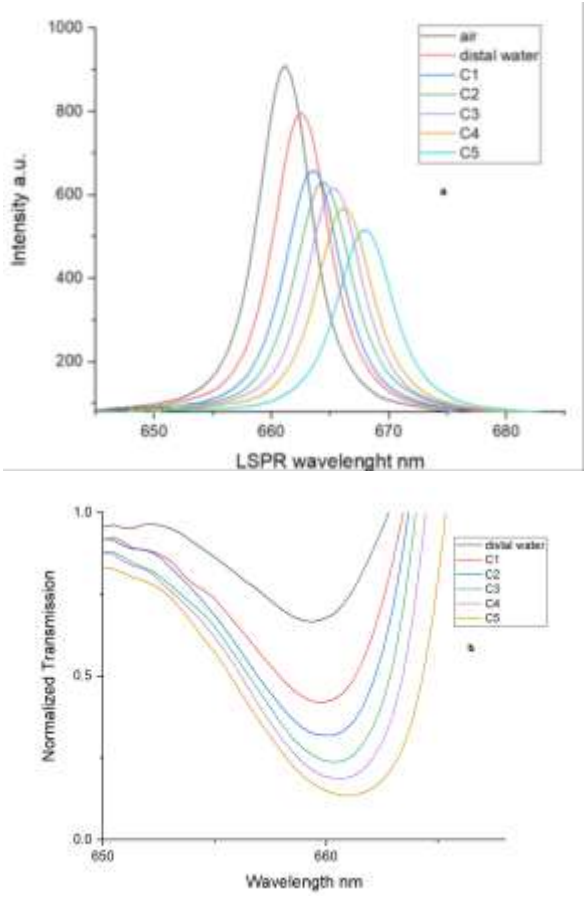

Figure 9: (a)

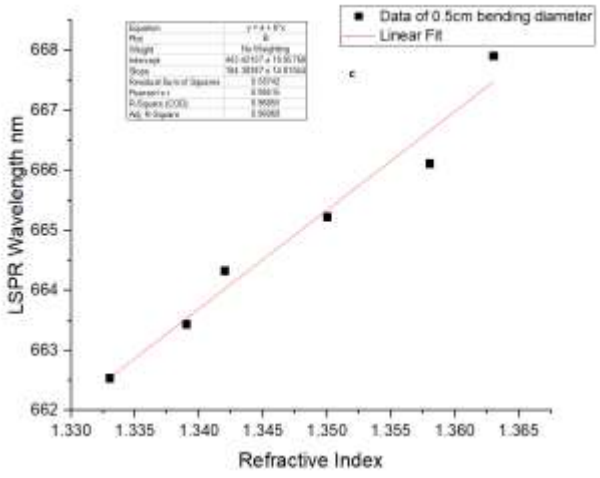

Response of U shape POF sensor with 0.5 cm bending diameter with 20 nm GNPs thickness. (b) Normalized Transmission spectrum. (c) Linear fitting curve.

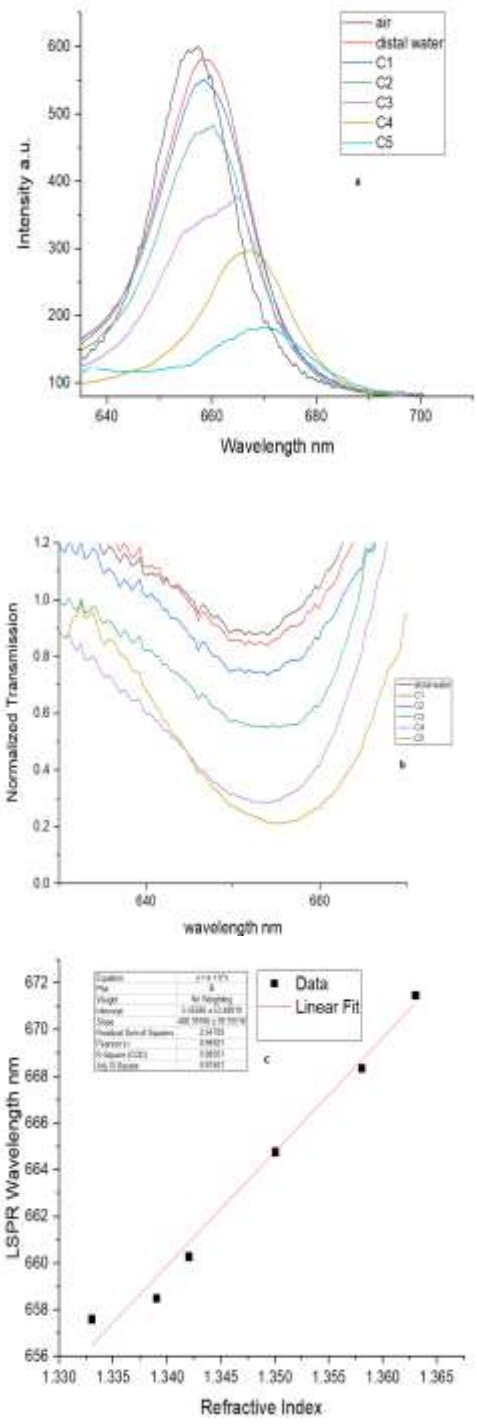

Figure10: (a) The response intensity of U shape sensor with 0.5 cm bend diameter coated with 30 nm thickness of GNPs immersed in different concentrations of NaCl solution. (b) Normalized transmission. (c) Linear Fitting curve.

It can be observed in figure 10a that 14 nm red shift of LSPR wavelength with increase the sodium chloride solution concentrations at room temperature, the red shift of the local resonance wavelength get larger due to addition more thickness of GNPs. In figure 10 c the sensor response to refractive index change was found to be linear with R^2=0.98 and higher sensitivity of 466.66 nm/RIU was obtained. This occurs because the increase in GNPs thickness allows more significant interaction between surface Plasmon mode and fiber mode that giving an SPR resonant wavelength more shift[4] [15]. These findings is agreement with results of the study in reference[16], [4] and [10] (For various RI solutions, the probes with increased film thickness show strong SPR wavelength sensitivity).

The change in resonance wave length with change in refractive index of sensing media can explain by the principles of SPR and the intensity decreasing occurs because the increased concentration of outside solution increases absorption of light power by the solution resulting in decreasing in the intensity of light because U bent sensor based on Intensity modulation.

The normalized transmission curves that shown in figures 9b and 10 b that the higher concentration of the solution, the greater depth of the transmittance curves with red wavelength shift because the LSPR phenomena was occurred. Normalized transmission curves were calculated from transmittance equation: $T = \frac{I_{out}}{I_{in}}$

Transmittance is unit less. Where I_{in} is the reading of intensity for air, I_{out} is the reading of intensity for solutions.

Table (1): Compering the sensitivity between some optical LSPR sensors.

Sensor type	Material	sensitivity nm/RIU	Reference
D shape fiber	GNPs	580	[17]
U bent fiber	MoS2 -gold film	6184.4	[18]
U bent fiber	Gold nanoparticles	466.66	This work

4. Conclusion:

In this study, a U-shaped fiber-optic sensor was built using a plastic optical fiber with a curvature diameter of 0.5 cm, and part of the fiber's outer cortex was removed in the bending region to become a D-shape. This sensor was tested on sodium chloride solution with refractive index change from1.333-1.363 and it was noted that the wavelengths do not shift, but the intensity decreases with increasing concentrations of the sodium chloride solution. When the sensor was coated with gold nanoparticles with a thickness of 20 nm, a red shift of wavelengths was observed by 5.12 nm with an increase in the concentration of sodium chloride solution and 179 nm/RIU obtained sensitivity, for coating the sensor with 30 nm thick gold nanoparticles, a wavelength shift of 14nm was observed with increasing concentrations of sodium chloride solution and a higher sensitivity of 466.66 nm/RIU was obtained. The coating with GNPs enhanced the sensitivity for the sensor. This sensor is simple, has good detection specificity and excellent reliability, it can be used in bio/chemical applications.

References:

[1] M. M. Hasan and H. J. Taher, "The Influence of No-Core Fiber Length on the Sensitivity in Fiber Optic Strain Sensor," *Iraqi J. Laser*, vol. 20, no. 1, 2021.

[2] S. L. Kashen and H. J. Taher, "The influence of no-core fibre length on the sensitivity Optical fibre Humidity sensor," *Iraqi J. Laser*, vol. 20, no. 2, pp. 18–23, 2021.

[3] S.-K. Liaw, "Introductory Chapter: An Overview the Methodologies and Applications of Fiber Optic Sensing," *Fiber Opt. Sensing-Principle, Meas. Appl.*, 2019.

[4] C. Christopher, A. Subrahmanyam, and V. V. R. Sai, "Gold Sputtered U-Bent Plastic Optical Fiber Probes as SPR- and LSPR-Based Compact Plasmonic Sensors," *Plasmonics*, vol. 13, no. 2, pp. 493–502, 2018, doi: 10.1007/s11468-017-0535-z.

[5] M. S. Sada, B. R. Mahdi, H. Ali, N. A. Aljbar, and M. A. Mohammed, "Localized surface plasmon resonance based photonic crystal fiber for cadmium detection," *NeuroQuantology*, vol. 19, no. 7, pp. 187–195, 2021, doi: 10.14704/nq.2021.19.7.NQ21102.

[6] H. Song, H. Zhang, Z. Sun, Z. Ren, X. Yang, and Q. Wang, "Triangular silver nanoparticle U-bent fiber sensor based on localized surface plasmon resonance," *AIP Adv.*, vol. 9, no. 8, 2019, doi: 10.1063/1.5111820.

[7] S. K. Al-Hayali, A. M. Salman, and A. H. Al-Janabi, "High sensitivity balloon-like interferometric optical fiber humidity sensor based on tuning gold nanoparticles coating thickness," *Meas. J. Int. Meas. Confed.*, vol. 170, p. 108703, 2021, doi: 10.1016/j.measurement.2020.108703.

[8] M. H. Tu, T. Sun, and K. T. V Grattan, "Optimization of gold-nanoparticle-based optical fibre surface plasmon resonance (SPR)-based sensors," *Sensors Actuators B Chem.*, vol. 164, no. 1, pp. 43–53, 2012.

[9] A. da S. Arcas, F. da S. Dutra, R. C. S. B. Allil, and M. M. Werneck, "Surface plasmon resonance and bending loss-based U-shaped

plastic optical fiber biosensors," *Sensors*, vol. 18, no. 2, p. 648, 2018.

[10] T. Xie, Y. He, Y. Yang, H. Zhang, and Y. Xu, "Highly Sensitive Surface Plasmon Resonance Sensor Based on Graphene-Coated U-shaped Fiber," *Plasmonics*, vol. 16, no. 1, pp. 205–213, 2021, doi: 10.1007/s11468-020-01264-x.

[11] A. J. Y. Tan, S. M. Ng, P. R. Stoddart, and H. S. Chua, "Theoretical model and design considerations of U-shaped fiber optic sensors: A review," *IEEE Sens. J.*, vol. 20, no. 24, pp. 14578–14589, 2020.

[12] S. Wang, D. Zhang, Y. Xu, S. Sun, and X. Sun, "Refractive index sensor based on double side-polished u-shaped plastic optical fiber," *Sensors (Switzerland)*, vol. 20, no. 18, pp. 1–13, 2020, doi: 10.3390/s20185253.

[13] N. J. de Mol and M. J. E. Fischer, "Surface Plasmon Resonance: Methods and Protocols," *Life Sci.*, p. 255, 2010, doi: 10.1007/978-1-60761-670-2.

[14] B. Gholamzadeh and H. Nabovati, "Gholamzadeh e Nabovati - 2008 - Fiber Optic Sensors," vol. 2, no. 6, pp. 1107–1117, 2008.

[15] M. Iga, A. Seki, and K. Watanabe, "Gold thickness dependence of SPR-based hetero-core structured optical fiber sensor," *Sensors Actuators, B Chem.*, vol. 106, no. 1 SPEC. ISS., pp. 363–368, 2005, doi: 10.1016/j.snb.2004.08.017.

[16] J. Satija, N. S. Punjabi, V. V. R. Sai, and S. Mukherji, "Optimal design for U-bent fiber-optic LSPR sensor probes," *Plasmonics*, vol. 9, no. 2, pp. 251–260, 2014, doi: 10.1007/s11468-013-9618-7.

[17] N. Cennamo *et al.*, "Localized surface plasmon resonance with five-branched gold nanostars in a plastic optical fiber for bio-chemical sensor implementation," *Sensors (Switzerland)*, vol. 13, no. 11, pp. 14676–14686, 2013, doi: 10.3390/s131114676.

[18] H. Song, Q. Wang, and W.-M. Zhao, "A novel SPR sensor sensitivity-enhancing method for immunoassay by inserting MoS2 nanosheets between metal film and fiber," *Opt. Lasers Eng.*, vol. 132, p. 106135, 2020.

دراسة تاثير سمك طلاء الذهب على حساسية مستشعر الليف البصري بشكل U على ظاهرة تردد الرنين السطحي الموقعي

سفانة ذياب مسير, بشرى رزوقي مهدي

معهد الليزر للدراسات العليا ، جامعة بغداد ، بغداد ، العراق

الملخص: في هذا البحث ، تم تصميم وتنفيذ متحسس الياف بصرية المعتمد على ظاهرة رنين البلازمون السطحي الموقعي حيث تم تصنيع المتحسس باستخدام ليف بصري بلاستيكي وتم عمل انحناء له على شكل U بقطر انحناء مقداره 0.5 سم. ثم عمل صقل لراس المتحسس عند منطقة الانحناء ليكون شكل المقطع العرضي للفايبر على الشكل D. تم اختبار هذا المتحسس على محلول ملح كلوريد الصوديوم بمعامل انكسار يتراوح من 1.333 الى 1.363. ثم تم طلاء المتحسس بجزيئات الذهب النانوية بسمك 20 nm وتم اختباره على نفس محلول ملح كلوريد الصوديوم. ثم تم طلاءه بجزيئات الذهب النانوية بسمك 30nm للحصول على اعلى حساسية تبلغ 466.66 nm/RIU

Iraqi J. Laser, issue 2, vol., 21, pp. 25-32 (2022)

IRAQI JOURNAL OF LASER

Design Optical BPF Using Double Clad Fiber MZI for Free Space Optical Communication

Mohanad G. Khamees [1, 2] , Tahreer S. Mansour [1,*]

**Corresponding author: Tahreer@ilps.uobaghdad.edu.iq*

1. Institute of Laser for Postgraduate Studies, University of Baghdad, Baghdad, Iraq.
2. Computer Engineering Departmen, Al Farabi University College, Baghdad, Iraq

(Received 27/7/2022; accepted 31/8/2022)

Abstract: A novel design of Mach Zehnder Interferometer (MZI) in terms of using special type of optical fiber that has double clad with graded distribution of the refractive index that can be easily implemented practically was suggested and simulated in this work. The suggested design is compact, rapid, and is simple to be modified and tested. The simulated design contains a MZI of 1546.74 nm of central wavelength that is constructed using special type of double clad optical fiber that has two different numerical apertures. The first aperture will supply single mode propagation via its core, while the second numerical aperture supports a zigzag wave propagation (multimode) in the first clad region. The interferometer's sensing arm (double clad fiber) was etched using 40% Hydro-Fluoric (HF) acid to achieve three different fiber diameters, which are (84, 72, 54) µm with (5) cm length. The simulation programs Optiwave version 15 and Optigrating version 4.2.2 were used to simulate the setup and to acquire the readings for the three durations of etching (10, 20, and 30) min, and also for the case of no etching at all. The obtained results show that the simulated setup can be used efficiently to test which one of the etching cases has the highest effect on the performance of the overall system, specifically when it comes to spectrum bandwidth, signal amplitude, and received power.

Keywords: Mach Zehnder Interferometer – Fiber Interferometer – Etched Double Clad Fiber – Optical Band Pass Filter

1. Introduction:

Novel integrated optics are currently regarded as the fundamental element of processing all types of light waves, where they can be utilized for both transmitting and receiving the data. That's the main cause that most new research directions are aimed at achieving the task of eliminating most electronic components in communication systems, where they are replaced by optical components instead to achieve better results [1, 2].

There are several applications for an optical system, such as implementing a system to produce a narrow laser pulse, which is considered as an important part in many optical setups [3]. There has been an exponentially increasing interest in designing novel photonic setups that can work with fast rates of data communication as well [4, 5].

An optical fiber interferometer is a photonic device that is used in many applications like optical Band Pass Filter (BPF), pulse compressor and super continuum generation optical source. Optical fiber MZI is a simple interferometer to be implemented practically.

Photonic devices group previously worked on designing optical fiber MZI as optical BPF using four different types of optical fibers: In 2018, Hollow Core Photonic Crystal Fiber (HC-PCF) with 7 and 19 cells were used [6], while in 2020 an optical fiber MZI was designed using Large Mode Area fiber (LMA-10) and two types of HC-PCF 7 and 19 cells after filling all their holes with ethanol, acetone, and acetic acid [7].

In 2022, an optical fiber MZI was designed using optical fiber with zero Polarization Mode Dispersion (PMD), which is called Polarization Maintaining Fiber (PMF) [8]. Lastly in 2022,

designed nested optical fiber MZI using three different etching times of Multi-Mode Fiber (MMF) [9].

In this work, the suggested approach covers a design and simulation of an optical system implemented by utilizing an MZI. The system is focused on a Double Clad (DC) optical fiber that is placed between two identical Single Mode Fibers (SMF's), which is different from No Core Fiber (NCF) and Dispersion Compensation Fiber (DCF) in that DC fiber supports single mode wave propagation at the core while simultaneously supports multimode wave propagation in the first cladding at the same time. The measurements are taken when the DC optical fiber is etched for (10, 20, and 30) minutes, and compared to the readings in the case when it is not etched at all as a reference.

2. Theoretical background:

Dispersion phenomena is a negative effect in the wave propagation via optical fibers which cause optical pulse broadening [10].

For the simulated setup, there is an Optical Spectrum Analyzer (OSA) component placed after each other component to check the effect of each stage on the spectrum of the light pulse. It is important to mention that the MZI is produced by the etched DC fiber that is placed between two SMF's, where the etching results in producing a mode misalignment [1, 11].

Interferometers can be used to give information regarding temporal, spatial, and spectral domains, so the received signal from them can be specified in a set of quantities [12].

This is a proper way in order to detect any changes that occurs to the several parameters of the light pulse, such as frequency, bandwidth, and other parameters [12].

It should be mentioned that the etching process affects the number of propagating modes within the optical fiber, that is because the clad size to core size ratio is affected [13].

3. Method and procedure:

It should be mentioned that the (HF) acid is usually used in optics laboratories since it has strong etching effect, and specifically when used on silica, which is the material most optical fibers are made from. So, the (HF) acid can be used for decreasing the diameter. This procedure is affected by the duration it is performed, which means that etching for a longer time period removes more thickness of the optical fiber layer compared to that removed in shorter time duration [14 – 18].

For the suggested simulated setup in this work, the diameter of the DC fiber is reduced by etching it using HF acid in three steps, where these steps are acquired by changing the etching time durations as (10, 20, 30) minutes. Setup consists of components that are described:

4. Simulated setup:

The setup that was simulated in this work is as shown below in figure (1)

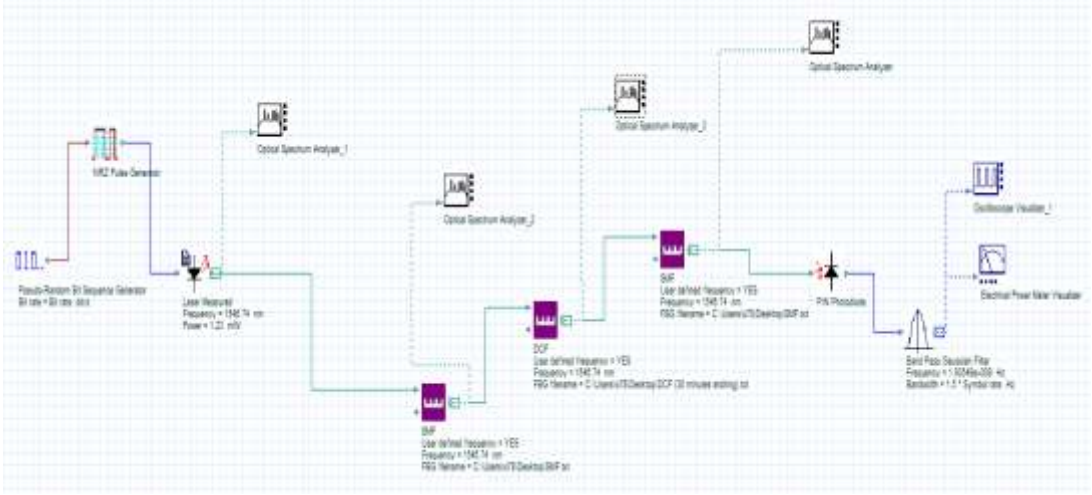

Figure (1): Schematic diagram of simulated setup.

4.1 Pseudo Random Bit Sequence Generator:
This generator is utilized to produce a random sequence of 1's and 0's to act as a power feeder to the laser source, that is because producing a laser is a random process.

4.2 NRZ Pulse Generator:
This generator is used to provide the necessary pulses encryption that is required by the laser source to operate properly

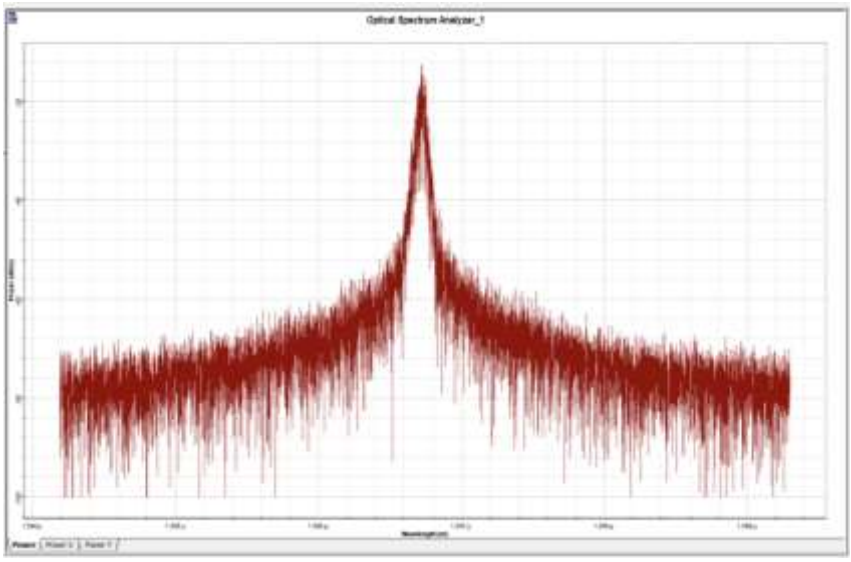

Figure (2): spectrum of laser source

4.3 Laser Measured:
This is the pulsed laser source in the setup, it has a peak power of 1.23 m. W, and a wavelength of 1546.74 nm. Its spectrum is as shown in figure (2)

4.4 SMF:
There are 2 SMF's in the setup, where each one of them is connected to one end of the DC fiber.

4.5 DCF:
This is the main component in the setup, where its diameter is changed 3 times and for each case, the readings are taken to acquire the desired results.

The default DC fiber without etching is as shown in figure (3) below, where it is considered as the first case of four cases. For each case, multiple readings are taken, including:

1- Power at the receiver.
2- Amplitude at the receiver.
3- The optical spectrum at various points.

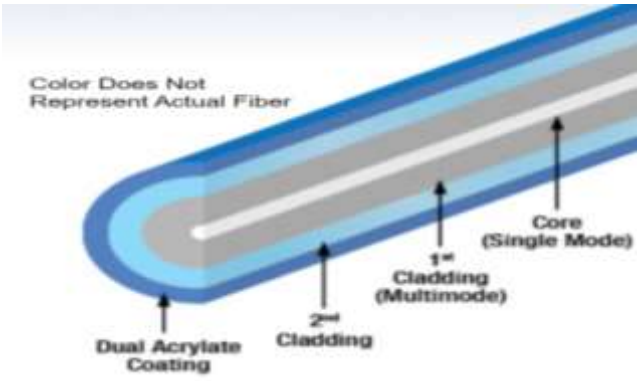

Figure (3): Schematic diagram of DC fiber.

4.6 PIN Photodiode:
Positive – Intrinsic – Negative (PIN) photodiode is used to detect the optical pulse by changing it from optical to electrical form, which means changing it from intensity to amplitude and power.

4.7 Band Pass Gaussian Filter:
This filter is utilized to take only the required spectrum into account, any part of the spectrum outside the frequency response of this filter will be attenuated and filtered out.

4.8 Optical Spectrum Analyzer:
There are several (OSA) components in the setup, where each one of them shows the spectrum of the pulse at a specific point. It is most useful to acquire information about power budget and bandwidth budget.

4.9 Electrical Power Meter Visualizer:
This visualizing component shows a numerical value, which is most useful when the power difference in two cases is rather low such that it is hard to be detected in graphical visualizers.

4.10 Oscilloscope Visualizer:
This component is used to acquire a visual reading of the amplitude of the pulse at the receiver end of the setup.

5. Results and discussion:
The simulated setup shown previously is run 4 times (one for each etching duration), and for each one of those times, the resulting graphs are shown, where figure (4) below shows the spectrum of the pulsed laser after passing through the 1st SMF.

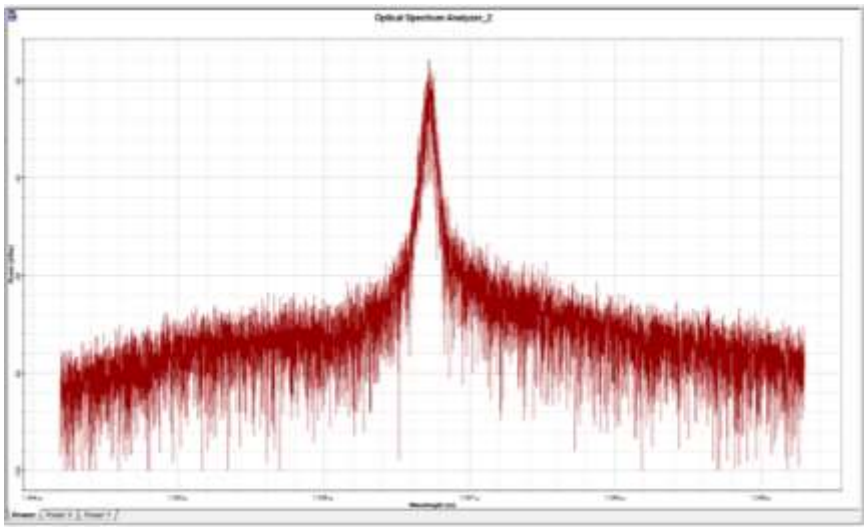

Figure (4): Spectrum of the pulsed laser after passing through first SMF

Figure (5) shown next illustrates that the attenuation of the etched DC fiber is affecting the spectrum of the pulse in a nonlinear fashion, where for example it is shown here that the peak power is reduced. It's important to mention that the spectrum suffers from attenuation in all parts, and not just the peak value.

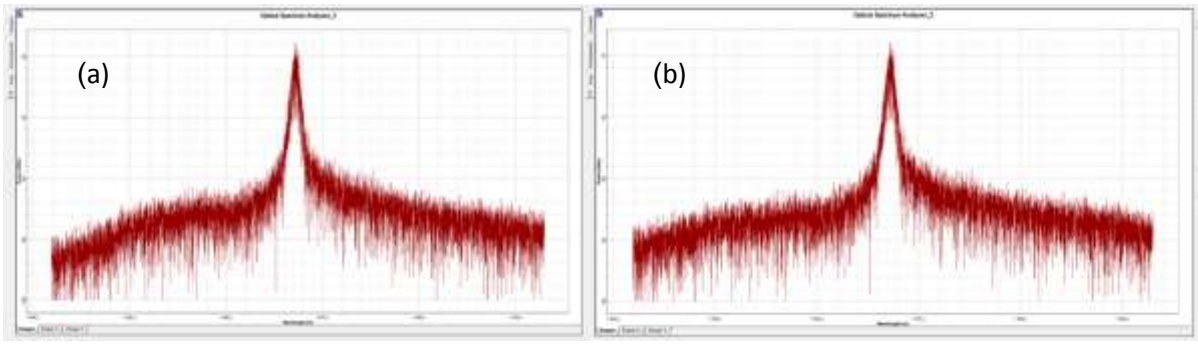

Figure (5 (a and b)): OSA after DC fiber for (a) no etching (b) etching for 10 minutes

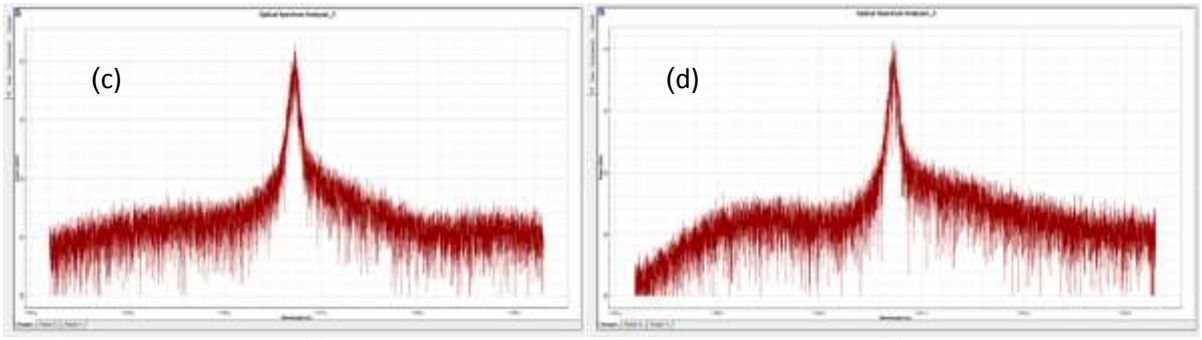

Figure (5 (c and d)): OSA after DC fiber for (c) etching for 20 minutes (d) etching for 30 minutes

Output peak power is an essential parameter for designing the optical BPF, which is affected by the attenuation characteristics of the optical fiber (0.2 dB/km in an SMF) and the other essential parameter in designing is dispersion, where it is (18 ps / nm . km). These two parameters are labelled in the c-band optical communication system. Figure (6) demonstrates that the 2nd SMF offers spectrum attenuation and slight dispersion as well, where the coupler is made from SMF-28 in any optical fiber visualizer.

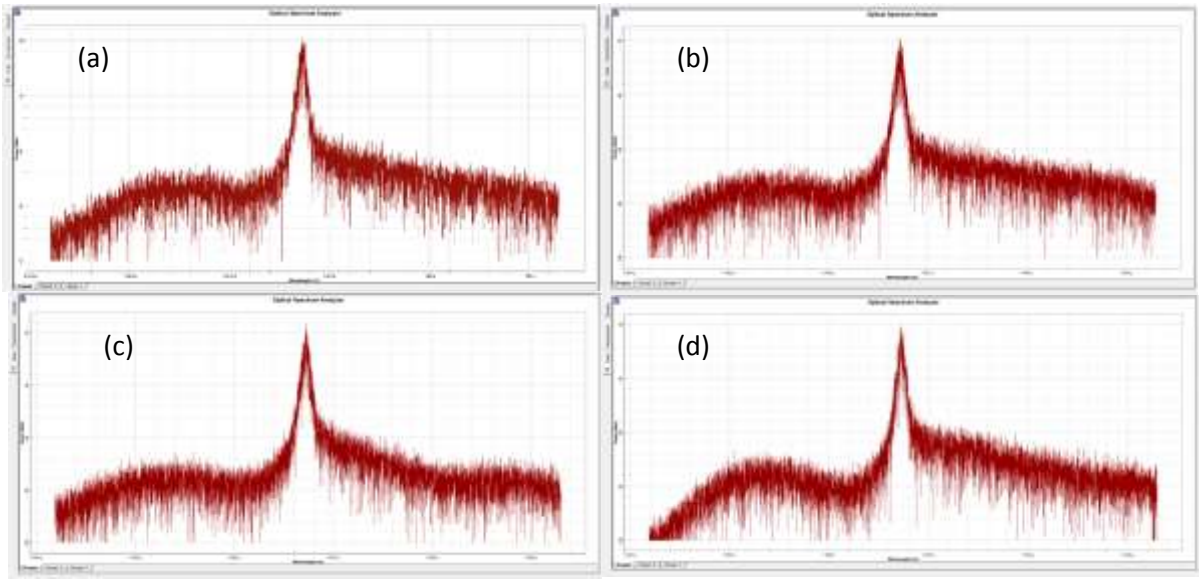

Figure (6): OSA after 2nd SMF for (a) no etching (b) etching for 10 minutes (c) etching for 20 minutes (d) etching for 30 minutes

Figure (7) here shows that the voltage peak to peak value gets affected as well by etching the DC optical fiber, where the lowest value here is for the etching duration of 20 minutes, that is because the effect is nonlinear regarding the etching time.

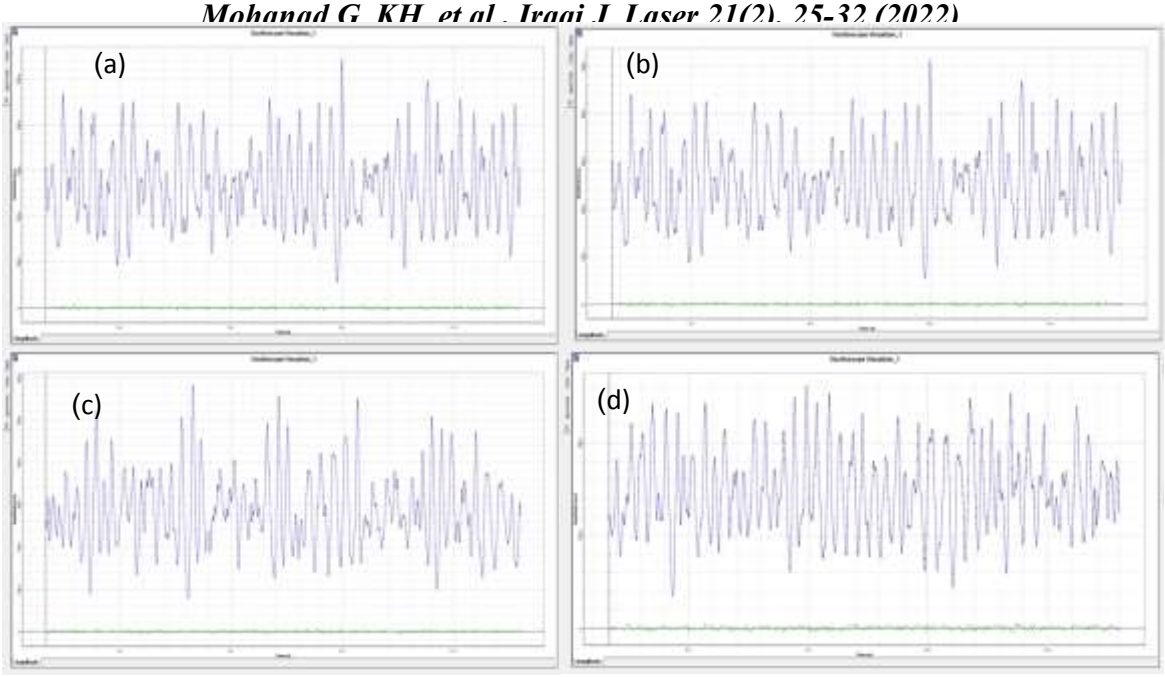

Figure (7): Oscilloscope after receiver for (a) no etching (b) etching for 10 minutes (c) etching for 20 minutes (d) etching for 30 minutes

The average power is altered as well by the effect of etching the DC optical fiber, which can be clearly seen from figure (8) below

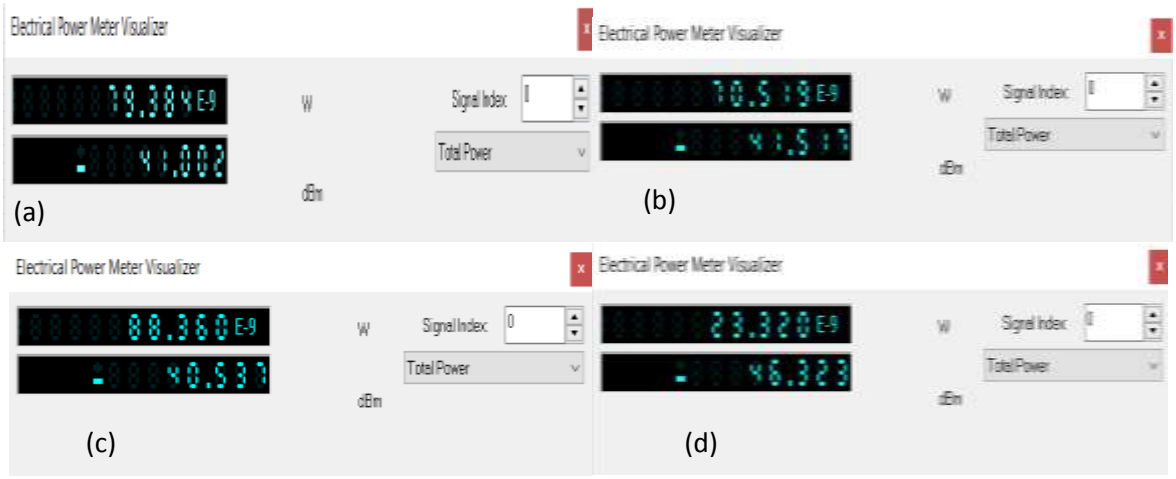

Figure (8): Power meter after receiver for (a) no etching (b) etching for 10 minutes (c) etching for 20 minutes (d) etching for 30 minutes

Table (1): Comparison between the four cases of etching durations

Case	Etching time (minutes)	Remaining diameter (μ. meters)	FWHM (n. meters)	Peak to Peak Voltage (n. Volts)	Peak Power (dBm)	Average power (n. Watts)
1	0	125	0.22	0.480	-18	79.384
2	10	84	0.21	0.460	-18	70.519
3	20	72	0.17	0.500	-17	88.360
4	30	54	0.20	0.225	-20	23.320

6. Conclusions

Narrow optical PBF was obtained from an etched DC fiber MZI that has 170 pm Full Width Half Maximum (FWHM) with highest average power of 88.36 n.W in the case of 20 minutes etching time, and a fiber length of 5 cm because the maximum excitation to the higher order modes in the second cladding region occurred, and the surrounding media is air, so four different refractive index distributions happened gradually from its highest value at core region (n = 1.5247) to its lowest value of surrounding media (which is air n =1)

References

[1] Tahreer S. M., Nada F. N., "Design and Construction of Tunable Band Pass Filter Using Hybrid FPMZI", Design Engineering, 4187, 6959-6972 (2021)

[2] Govind P. Agrawal, "Nonlinear application of fiber optics", Academic Press, New-York (2007)

[3] Mutar B. H., Noori N. F., Hammadi Y. I., & Mansour T. S., "In-line fiber tunable pulse compressor using PM-Mach Zehnder interferometer", Journal of Mechanical Engineering Research and Developments, 44, 287–297 (2021)

[4] Nada F. Noori, Tahreer S. Mansoor, "Experimental Study to The Effect of Applying Stressing Force on Etched Polarization Maintaining Fiber as Hybrid Fabry-Perot /Mach- Zehnder inline fiber interferometer", Iraqi J. Laser, 20, 2, 24-31 (2021)

[5] Tahreer S. Mansoor, Nada F. Noori, "Theoretical and Experimental Study to The Effect of Etching on Polarization Maintaining Fiber of Mach-Zehnder interferometer", Design Engineering, 4188, 6973-6981 (2021)

[6] Sura H. Mahmood, "Pulse compression using tunable etalons Fabry – Perot photonic crystal fiber", Thesis submitted to ILPS (2018)

[7] Ali A. Dawood, "Design and implementation of inline fiber pulse compression using photonic crystal fiber", Thesis submitted to ILPS (2020)

[8] Baraa H. Mutar, "Pulse Compression using polarization maintaining fiber Mach-Zehnder interferometer", Thesis submitted to ILPS (2021)

[9] Asmaa A. Abdulwahab, "Design and implementation of multi-mode fiber Mach-Zehnder interferometer for sensor network", Thesis submitted to ILPS (2021)

[10] K.S. Shuraavi and A. Fairooz, "Optical Fiber - Dispersion, Construction, Application, Technology, Future" (2016)

[11] Tao Zhu, Di Wu, Min Liu, and De-Wen Duan, "In-Line Fiber Optic Interferometric Sensors in Single-Mode Fibers", sensors, ISSN 1424-8220, review article, vol. :12, issue:10430-10449; doi:10.3390/s120810430

[12] Korposh S., James S. W., Lee S. W., & Tatam R. P., "Tapered Optical Fibre Sensors: Current Trends and Future Perspectives", Sensors Switzerland, 19(10), doi.org/10.3390/s19102294 (2019)

[13] John Senior, M. Yousif Jamro," Optical Fiber Communications Principles and Practice", Third edition, Prentice Hall Europe, ISBN: 978-0-13-032681-2 (2009)

[14] Alsweefe H., Al-Hayali S. K., & Al-Janabi A, "Efficient humidity sensor based on an etched no-core fiber coated with copper oxide nanoparticles", Journal of Nanophotonics, 12(04), https://doi.org/10.1117/1.jnp.12.046018 (2018)

[15] Patil S. H., Saha A., & Barma M. D., "Performance analysis of cladding etched fiber Bragg grating based refractive index sensor", 2nd International Conference on Electronics, Materials Engineering and Nano-Technology, IEMENTech, 6, 1–3, https://doi.org/10.1109/ IEMENTECH.2018.8465251 (2018)

[16] Pallarés Aldeiturriaga D., Roldán-Varona P., Rodríguez-Cobo L., and López Higuera J. M., "Optical fiber sensors by direct laser processing: A review", Sensors (Switzerland), 20(23), 1–37, https://doi.org/10.3390/s20236971 (2020)

[17] Flores R., Janeiro R., & Viegas J., "Optical fibre Fabry-Pérot interferometer based on inline microcavities for salinity and temperature sensing", Scientific Reports, 9(1), 1–9, https://doi.org/10.1038/s41598-019-45909-2 (2019)

[18] Kumar A., "Single Mode Optical Fiber based Refractive Index Sensor using Etched Cladding", 0 – 4, https://doi.org/10.21427/wh9t-ce84 (2011).

تصميم فلتر ضوئي من نوع معبر الحزمة الوسطية بإستخدام مُداخل ماخ زندر من ليف ضوئي ثنائي الغلاف للإتصالات الضوئية في الفضاء الحر

مهند غازي خميس تحرير صفاء منصور

معهد الليزر للدراسات العليا / جامعة بغداد – بغداد / العراق

الخلاصة: تصميم لمنظومة مُداخل ماخ-زندر ريادي من ناحية إستعمال نوع مميز من الليف الضوئي ذو الغلاف المزدوج يحتوي على توزيع متدرج لمعامل الإنكسار والذي من الممكن تنفيذه ببساطة بشكل عملي تم اقتراحه ومحاكاته في هذا العمل. التصميم المقترح صغير، وسريع، ومن السهل التعديل وإجراء الفحوصات عليه.

التصميم المُحاكى يحتوي على مُداخل ماخ-زندر ذو طول موجي يبلغ مركزه ١٥٤٦.٧٤ نانومتر الذي تم بناؤه من نوع مميز من الليف الضوئي ذو الغشاء المزدوج الذي يحتوي على قيمتان مختلفتان من الفتحات العددية. الفتحة العددية الأولى سوف تدعم إنتشار أحادي الطور بواسطة مركز الليف، أما الفتحة العددية الثانية فتدعم الإنتشار الموجي المتعرج (متعدد الأطوار) في منطقة الغشاء الأول. الذراع المتحسسة الخاصة بالمُداخل (الليف الضوئي ذو الغشاء المزدوج) تم حكها بإستخدام 40% حمض هيدروفلوريد للحصول على ثلاثة قيم مختلفة للأقطار، وتبلغ (٨٤، ٧٢، ٥٤) مايكرومتر بطول قدره 5 سم.

برامج المحاكاة (Optiwave 15 & Optigrating 4.2.2) تم استعمالها لمحاكاة المنظومة والحصول على القراءات للفترات الثلاث من الحك (١٠، ٢٠، ٣٠) دقائق، وأيضاً لحالة عدم الحك إطلاقاً. النتائج التي تم الحصول عليها تظهر بأن المنظومة التي تمت محاكاتها من الممكن استعمالها بكفاءة لفحص أي من حالات الحك لديها التأثير الأكبر على أداء النظام الكامل، وبالذات من ناحية عرض الحزمة، وفولتية الإشارة، والقدرة المستلمة.

Iraqi J. Laser, issue 2, vol., 21, pp. 33-40 (2022)

IRAQI JOURNAL OF LASER

S and U shape offset studying of the refractive index sensor based on coreless fiber

Aya R. Mejble* Hanan J.Taher

*Corresponding author: ***Aya.riadh1201a@ilps.uobaghdad.edu.iq***

Institute of Laser for Postgraduate Studies, University of Baghdad, Baghdad, Iraq

(Received 13/8/2022; accepted 21/11/2022)

Abstract: Two different shapes of offset optical fiber was studied based on coreless fiber for refractive index (RI)/concentration (con.) measurement, and compare them. These shapes are U and S-shapes, both shapes structures were formed by one segment of coreless fiber (CF) was joined between two single mode (SMF) lead in /lead out with the same displacement (12.268µm) at both sides, the results shows the high sensitive was achieved in a novel S-shape equal 98.768nm/RIU, to our knowledge, no one has ever mentioned or experienced it, it's the best shape rather than the U-shape which equal 85.628nm/RIU. In this research, it was proved that the offset form has a significant effect on the sensitivity of the sensor. Additionally, the sensor is produced using a low-cost fabrication technique. Therefore, the suggested structure is advantageous for RI/ (con.) sensing applications.

Keywords: offset, RI sensor, concentration, S-shape, U-shape.

1. Introduction

Liquid refractive index (RI) assessment is crucial for a variety of applications, including environmental monitoring [1], food safety [2], and medical diagnostics [3]. The benefits of optical fiber-based RI sensors are resistance to electromagnetic interference, small size, high sensitivity, quick response, corrosion resistance, and availability for remote sensing [4].Numerous optical fiber-based RI sensor types have been proposed up to this point, such as the Plasmon resonance at the optical fiber surface [5], the optical fiber Bragg grating [6] , photonic crystal fiber [7-8].But to fabricate this kind of sensors mentioned requires a high cost and time consuming. In recent times, Mach-Zehnder interferometers (MZIs) in-line fibers have gained more and more attention due to their ease of fabrication. Different configurations of fiber-based MZIs have been claimed such as the two tapered fiber structure [9], long-period grating pairs [10], the two peanut fiber structure [11], double cladding [12] (PCF)[13-14], femtosecond laser-assisted partial fiber ablation[15].However, these RI sensors based on these structures do not have sufficient sensitivity. Even though increasing the sensitivity by chemically etching or decreasing the fiber diameter [16]. As a result, the sensor loses a lot of its mechanical strength and becomes brittle. Coreless offset fiber is one quick and easy way to create optical fiber RI sensors that have good mechanical strength and

high sensitivity. A number of offset fiber RI/(con.) sensors have recently been introduced based on: fiber types spliced such as single mode fiber (SMFs),multimode fiber (MMF), photonic crystal fiber(PCF) and coreless fiber(CF), based on shape offset including U-shape and S-shape , and based on side offset, this displacement site means in one or two sides. In this research, the RI sensor was studied based on offset shape and the (CF) with both sides' displacements. In this paper, the effect of the displacement shape on the sensitivity of the refractive index sensor was studied to find out which one is better; S-shape or U-shape, the results showed that the S-Shape has a higher sensitivity than the U –shape. The suggested sensor has the benefits of high sensitivity, straightforward design, straightforward production, and inexpensive cost.

2. Fabrication Principle and Sensing Structure

The configuration of the sensor was consist of one segment of CF (the coreless fiber is a special type of multimode fiber with uniform refractive index 1.46 (thorlabs)) was spliced between two SMFs lead in /lead out to be the (SCS) structure with fixed offset at both sides and two different shapes (U and S-shape) of sensor at the same best length which at CF 6 cm according to our previous work [17]. In this research the CF will be act as sensing segment and will be considered as a core and the environment as the cladding. To configure the U and S-shaped sensor, a fusion splicer with manual mode was used with some steps in fusion splicer as follows, a step one chose the splice mode for offset, in step two the set button was pressed (manual align) to choose motor x to control the amount of the offset, step three after the displacement amount has been determined, the button arc was pressed. With regard to the shape of the U when the ends of the fibers in the V-groove in the fusion splicing machine were precisely aligned x-direction , which represents the first part of the splicing (SMF – CF) with offset 12.268μm by displacing the CF (to down) and fixing the SMFs/lead in and this part (SMF-CF) was spliced with SMFs/lead out at the same offset with the first part(SMF-CF) remaining on the same side(left side) of the Fusion splicing(displacing SMF-CF, and fixed SMF/lead out to create the second part of the sensor and complete the U-shape, as for the shape of the S, the same steps as the U-shape but SMFs/lead out displacing to up with the same offset. An approximately Gaussian-shaped field intensity distribution is carried by light that enters the CF and moves along the lead-in SMF, at the first joint fiber (first offset) the light is, three optically pathways are created from the optical signal I_1: along the cladding of CF , and the other in the surrounding area near the surface of CF , At the second splice joint, they are then rejoined into the core at the SMFs lead out so as to create interfering fringe, which can be identified by measuring I_{out} .Given that light is passing through the sensor, as the RI of the environment varies with variations in the concentration of the solution used, it is evident that the optimum propagate constant of the cladding modes could change, so that we may measure the phase shift of the interference fringe and use the MZI fiber as a RI/(con.) sensor. When the following condition is met, the interference signal is at its lowest phase difference between cladding and core modes [18].

$$2\pi\left[n_{e\mathrm{ff}}^{co}-n_{e\mathrm{ff}}^{cl,j}\right]\frac{L}{\lambda D}=(2k+1)\pi \qquad (1)$$

Where λ_D denotes the interference spectrum dip's wavelength, $n_{e\mathrm{ff}}^{co}$ is the core mode's effective RI, $n_{e\mathrm{ff}}^{cl,j}$ is the effective RI of the j'th order cladding mode, L is the interferometer length, and k is an integer. Consequently, the sensitivity can be stated as follows [9]:

$$\frac{d\lambda D}{dnext}=\frac{-\lambda D}{\Delta neff}\frac{\partial n_{eff}^{cl;j}}{\partial next}\Big/\left[1-\frac{\lambda D}{\Delta n_{e\mathrm{ff}}}\left(\frac{\partial n_{eff}^{co}}{\partial\lambda}-\frac{\partial n_{eff}^{cl,j}}{\partial\lambda}\right)\right] \quad (2)$$

Where next is the RI of the surrounding medium, and Δneff is the distinction between

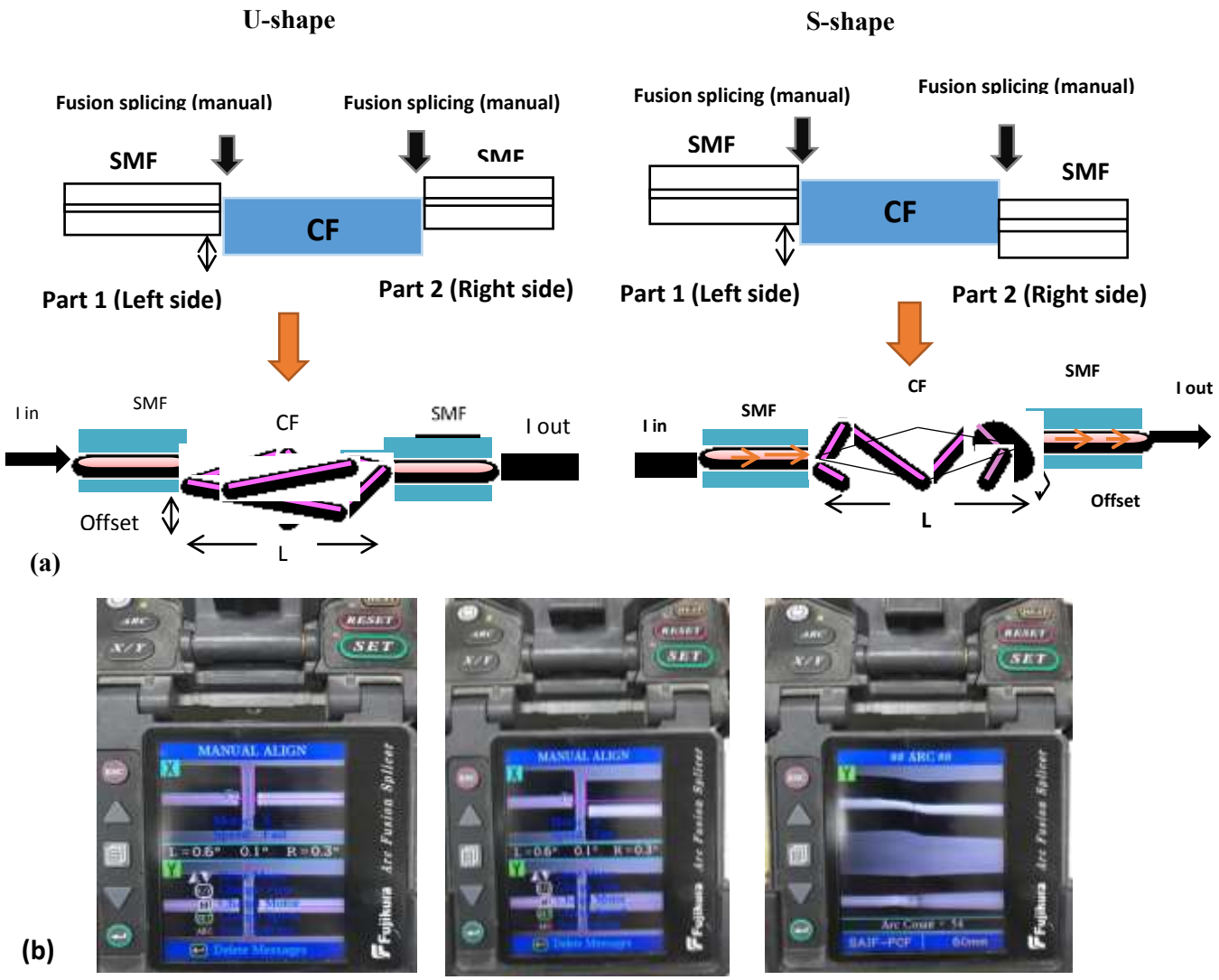

Figure (2) (a): the steps that go into fabrication the suggested sensor.
(b): picture captured from a splicing machine demonstrating an offset splicing.

3. Experimental Setup The experimental setup for the suggested RI/ (con.) sensor based on the offset SCS fiber structure shows the conceptual framework Fig.2, one end of the structure was linked to the cores and the claddings effective RIs.Fig.1 depicts graphically the suggested sensor structure. A broadband light source (B.B.S), the other end was spectrum of the sensors in different concentration of sodium chloride (NACL) (5%, 10%, 15%, 20%, 25%). The structure was placed in u-groove, and fixed the sensor by two holders as shown in Fig. 2.to kept the sensor from any bending and strain during the experiment.

Few drops of the NACL solution were distilled along the SCS structure until it was completely submerged, this process was repeat with each concentration of the NACL, and same experience for both sensors U, S-shape to study the effect shape offset sensor on sensitivity and compare them.

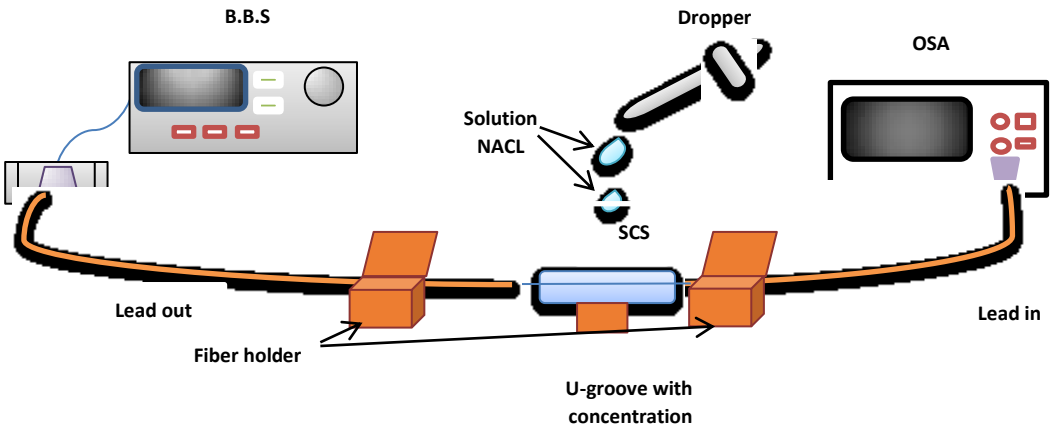

Figure (2): The schematic of the experiment setup

4- Experimental Results and Discussion

The RI/ (con.) response of the SCS (U, S-shapes) fiber structure (with offset in both sides at the same displacement 12.268 µm as shown Fig.3, and the same length of the CF 6 cm) toward the ambient RI/ (con.) was investigated. The RI was increased from 1.33 to 1.38 with increasing the (con.) of the NACL from (0% to 25%), It was made by weighing different NaCl powder concentrations (5, 10, 15, 20 and 25 gm) using an electrical scale to achieve greater accuracy. Each of these concentrations was dissolved in 100 ml of deionized water by a magnetic stirrer at room temperature (25 °C). The RI of each concentration of NACL solution is shown in table1 [19]. Fig.4 was shown the change of NACL conc. with refractive index of each con. . The transmutations spectra of each sensor (U, S-shapes) were recorded as shown as Fig. 3, where there was a clear indication of the spectral red shift. The shift in wavelengths was from 1604.455 to 1617.037 nm as shown in Fig. 4, the transmission spectra response shifted toward the longer wavelength (red shift) as the RI/(con.) of the surrounding was increased.

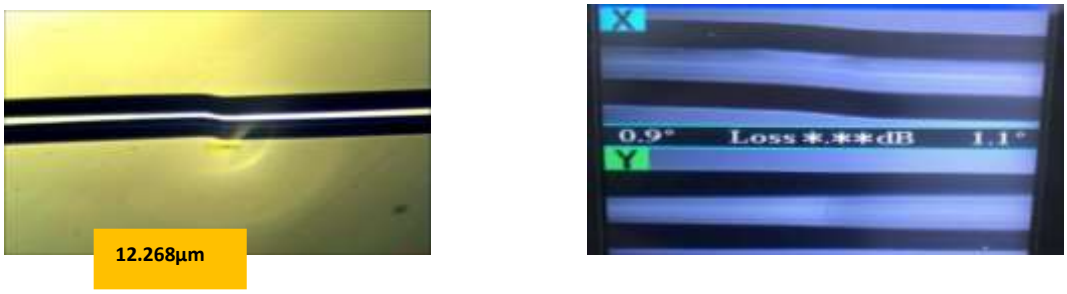

Figurer(3): (a) image the offset rejoin under the microscope (b) Image captured by a splicing device demonstrating an offset splice between SMF and CF coming from the x-direction (up) and the y-

Table 1: The refractive indices of the NaCl concentrations

The NaCl concentrations (%)	RI (RIU)
0%	1.33
5%	1.34
10%	1.35
15%	1.36
20%	1.37
25%	1.38

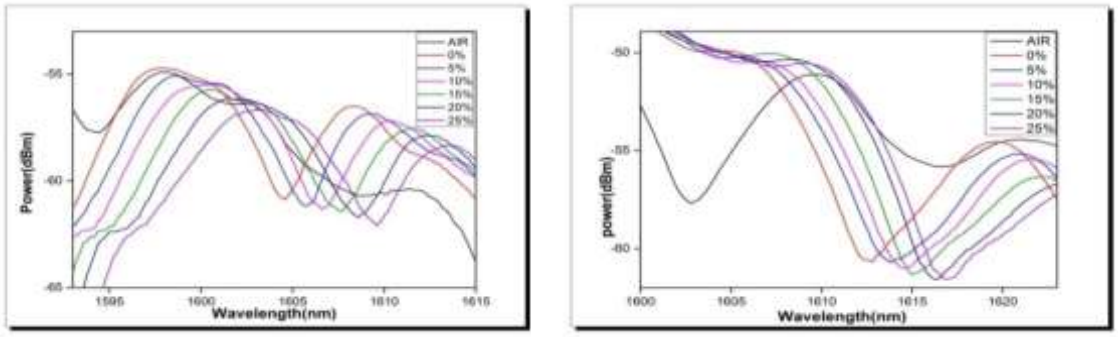

(a) (b)

Figure (4): Transmission spectra of two different offset shape (a) S-shape (b) U-shape

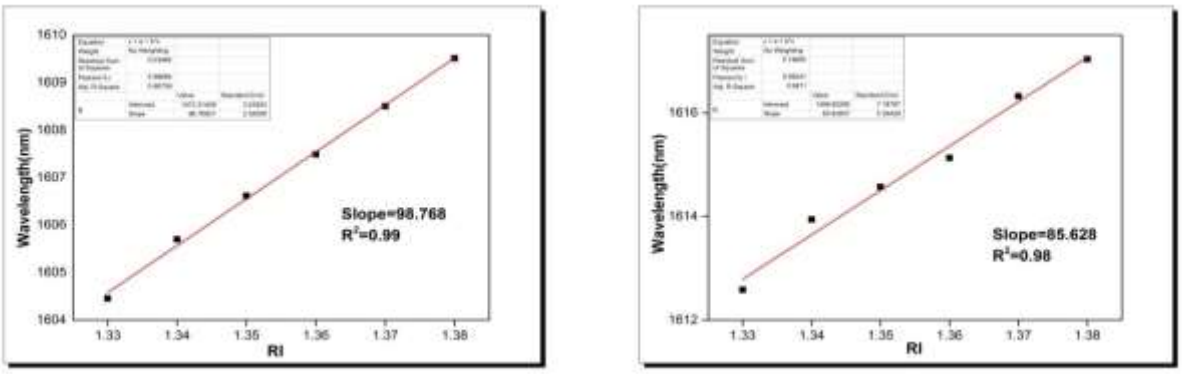

(a) (b)

Figure (5): The fitting linear of two offset shapes (a) s-shape (b) u-shape

The sensitivity of each sensor was calculated. Where the S-shaped sensor was more sensitive than the U-shape sensor as shown in Fig.5 which represented the fitting linear of these sensors The experiment results shows the high sensitive was achieved in a novel S-shape equal 98.768nm/RIU, to our knowledge, no one has ever mentioned or experienced it. It's the best shape rather than the U-shape which equal to 85.628nm/RIU, The reason for the high sensitivity of the S-shape sensor is due to more evanescent wave could be interact where there were more high order mode can be interference at two splicing area when the refractive index was increased from 1.33 to 1.38 [20]. Table 2 compares prior fiber MZI approaches in terms of length and RI sensitivity.

Table2 Comparison of the length and RI sensitivity of the various fiber MZI sensor approaches

Techniques	MZI length	RI sensitivitynm/RIU
Small offset(5µm)with tapered MZI[10]	**30 mm**	**78.7**
Small offset 6µm	**100mm**	**43.97**
Large offset 40 µm[21]	**70mm**	**123.40**
Small offset8.1 µm[22]38	**36mm**	**13.76**
This work	**6cm**	**98.76**

5. Conclusion

In this research, it was demonstrated that the shape of the sensor by using offset affects the sensitivity of the sensor, two shapes was studied (S and U-shapes), where it turns out that the S-shape is better than the U-shape, where the sensitivity of the S-shape is 98.786nm/RIU, while the U-shape is 85.628nm/RIU . The sensor was made in an easy and inexpensive way by attaching a piece of CF between two SMF lead in/lead out with displacement of 12.268µm at both sides.

Reference

[1] Joe, H. E., Yun, H., Jo, S. H., Jun, M. B., & Min, B. K. *"A review on optical fiber sensors for environmental monitoring"*. International journal of precision engineering and manufacturing-green technology, *5*(1), 173-191(2018)

[2] Patel, P. D. " *(Bio) sensors for measurement of analytes implicated in food safety: a review*". TrAC Trends in Analytical Chemistry, 21(2), 96-115(2002).

[3]Ahmed, K., Ahmed, F., Roy, S., Paul, B. K., Aktar, M. N., Vigneswaran, D., & Islam, M. S. *"Refractive index-based blood components sensing in terahertz spectrum" . IEEE Sensors Journal*, *19*(9), 3368-3375(2019).

[4] Bhardwaj, V., Kishor, K., & Singh, V. K. *"Experimental and theoretical analysis of connector offset optical fiber refractive index sensor". Plasmonics*, *12*(6), 1999-2004(2017)

[5] Slavík, R., Homola, J., & Čtyroký, J. *"Single-mode optical fiber surface plasmon*

resonance sensor". Sensors and Actuators B: Chemical, *54*(1-2),74-79 (1999).

[6] Iadicicco, A., Cusano, A., Cutolo, A., Bernini, R., & Giordano, M. *"Thinned fiber Bragg gratings as high sensitivity refractive index sensor". IEEE Photonics Technology Letters*, *16*(4), 1149-1151(2004).

[7] Wu, D. K., Kuhlmey, B. T., & Eggleton, B. J. *"Ultrasensitive photonic crystal fiber refractive index sensor". Optics letters*, *34*(3), 322-324(2009).

[8]Gangwar R, Singh VK *"Refractive index sensor based on selectively liquid fluid infiltrated dual core photonic crystal fiber"* .Photon Nano Str 15:46–52(2015).

[9] Zhang, Q., Zhou, J., Chen, J., & Tan, X. *"Single-mode fiber refractive index sensor with large lateral offset fusion splicing between two abrupt tapers". Optical Engineering*, *51*(9), 090502(2012)

[10] Chong, J. H., Shum, P., Haryono, H., Yohana, A., Rao, M. K., Lu, C., & Zhu, Y. *"Measurements of refractive index sensitivity using long-period grating refracto-meter". Optics communications*, *229* (1-6), 65-69(2004).

[11] Huang, R., Ni, K., Ma, Q., & Wu, X. *"Refractometer based on a tapered Mach–Zehnder interferometer with Peanut-Shape structure". Optics and Lasers in Engineering*, *83*, 80-82(2016) .

[12] Lvanov O, *Chertoriyskiy "Fiber-optic bend sensor based on double cladding fiber"*. J Sens. 726793–6(2015).

[13] H. Gong, C. Chan, F. Zhang, C. Wong, X. Dong, *"Miniature refractometer based on modal interference in a hollow-core photonic crystal fiber with collapsed splicing"*, J. Biomed. Opt. 16, 2–5(2011).

[14] C. Li, S. Qiu, Y. Chen, F. Xu, Y. Lu *"Ultra-sensitive refractive index sensor with slightly tapered photonic crystal fiber"*, IEEE Photon. Technol. Lett. 24, 1771–1774(2012).

[15] L. Zhao, L. Jiang, S. Wang, H. Xiao, Y. LuA *"high-quality Mach-Zehnder interferometer fiber sensor by femtosecond laser one-step processing"*, Sensors.11 , 54–61(2011).

[16] Coradin, F. K., Possetti, G. R., Kamikawachi, R. C., Muller, M., & Fabris, J. L. *"Etched fiber Bragg gratings sensors for water-ethanol mixtures: a comparative study". Journal of Microwaves, Optoelectronics and Electromagnetic Applications*, *9*, 131-143 (2010).

[17] A.R. mejbel and H. J.Taher *"Coreless fiber length influence for refractive index measurements based on lateral offset structure"*. Neuro Quantology 2022; 20(7):2337-2342(2022).

[18] Xia, T. H., Zhang, A. P., Gu, B., & Zhu, J. J. *"Fiber-optic refractive-index sensors based on transmissive and reflective thin-core fiber modal interferometers". Optics Communica-tions*, *283*(10), 2136-2139(2010)

[19] Zhao, Y., Li, X. G., & Cai, L." *A highly sensitive Mach–Zehnder interferometric refractive index sensor based on core-offset single mode fiber". Sensors and Actuators A: Physical*, *223*, 119-124(2015).

[20] Hamza, N. *Enhanced Refractive Index Sensor Based on Etched Coreless Fiber*. Authorea Preprints (2020).

[21] Yu, F., Xue, P., & Zheng, J. *Study of a large lateral core-offset in-line fiber modal interferometer for refractive index sensing*. *Optical Fiber Technology*, *47*, 107-112 (2019).

[22] Yao, Q., Meng, H., Wang, W., Xue, H., Xiong, R., Huang, B., & Huang, X. *Simultaneous measurement of refractive index and temperature based on a core-offset Mach–Zehnder interferometer combined with a fiber Bragg grating. Sensors and Actuators A: Physical*, *209*, 73-77(2014).

دراسة تأثير شكل الاوفسيت (S and U) على حساسية متحسس معامل الانكسار المعتمد على الليف البصري منزوع القلب

ايه رياض مجبل حنان جعفر طاهر

معهد الليزر للدراسات العليا / جامعة بغداد – بغداد، العراق

الخلاصه : تمت دراسة شكلين مختلفين من المتحسسات بناءا على شكل الاوفسيت (الازاحه الجانبيه) هما ال S و ال U وتأثيرها على متحسس معامل الانكسار المصنوع من ليف بصري منزوع القلب ذو طول 6سم تم لحامه بين ليفين بصريين احادي الطول الموجي بازاحه متساويه في كلا الطرفين وقدرها 12.268مايكرومتر بشكليين مختلفيين .لمعرفة مدى تاثير شكل الاوفسيت ع حساسية المتحسس , حيث اضهرت النتائج ان الحساسية الاعلى قد حققت في الشكل الجديد ال S الذي لم يسبق لاحد تجربته او صناعته على حد علمي , حيث كانت 98.768نانومتر/وحدات معامل الانكسار بينما حساسية ال U كانت تساوي 85.628نانومتر/وحدات معامل الانكسار.في هذا البحث تم اثبات ان شكل الاوفسيت يؤثر على حساسية المتحسس .بالاضافة الى ذلك ، يتم إنتاج المستشعر باستخدام تقنية تصنيع منخفضة التكلفة. لذلك ، فإن الهيكل المقترح مفيد لتطبيقات استشعار معامل الانكسار.

Iraqi J. Laser, issue 2, vol., 21, pp. 41-47 (2022)

IRAQI JOURNAL OF LASER

Cavity Disinfection Using Er,Cr:YSGG Laser Induced Photoacoustic Streaming Technique

Rand kareem Jassim Hussein Ali Jawad*

**Corresponding author: Hussein@ilps.uobaghdad.edu.iq*

Institute of laser for postgraduate studies, University of Baghdad, Baghdad, Iraq.

(Received 5/9/2022; accepted 21/11/2022)

Abstract:

Aim: The goal of this research was to study the influence of Er,Cr:YSGG laser at short pulse duration (60 µsec) on the number of streptococcus mutans bacteria in vitro.

Material and Methods: twenty-eight extracted third molars free of caries, cracks, and other irregularities were used. For the testing of the materials, both the agar well technique and a tooth cavity model were employed. The agar wells of plates that had been inoculated with Streptococcus mutans previously were stuffed with the test materials, in order to conduct the tests. The zones of inhibition were assessed using millimeter measurements, after an incubation period of 48 hours .In order to accomplish the tooth cavity model test, cylindrical cavities were invented in the occlusal surface of the teeth, which was kept even. The teeth were stored for 72 hours at 37°C in a broth culture of Streptococcus mutans. Following this, the teeth were divided arbitrarily into four groups of seven teeth (each including 14 cavity preparations). The experimental cavities in the first group (A) were not treated and considered as a control. In group B, a cavity disinfectant based on chlorhexidine was applied to the experimental cavities for 60 seconds. In group C, an erbium, chromium doped yttrium scandium gallium garnet laser was used at a short pulse duration (60 µsec) (0.25 watts, 15 Hz, 1% air, 1% water). In the last group, a chlorhexidine cavity disinfectant was applied for 60 seconds, followed by a laser treatment for 30 seconds with the same parameters as those described previously. The teeth were stored in saline for a period of three days. Standard amounts of dentin chips were retrieved from the cavity walls. ANOVA test was used to analyze repeated measure mean between tested concentration and control. Data expressed as mean ±SE. LSD tests was used to calculate the significant differences between tested mean.

Result: After the statistical test, the highly significant difference in the diameter of inhibition zone was observed in group D (26 mm) where both chlorhexidine and laser were used followed by group B (18.71 mm) where the chlorhexidine gluconate based cavity disinfectant used alone, the least significant difference observed in group C (10.26mm) where the laser used alone.

Conclusion: According to this in vitro study, a photon-induced photoacoustic streaming technique using an Er,Cr:YSGG pulse laser at short pulse duration effectively agitates a chlorhexidine-based cavity disinfectant, which leads to the inhibition of Sterptococcus Mutans.

Keywords: Er,Cr:YSGG ,PIPS, Strep.Mutans, Inhibition.

1. Introduction

The primary goal of caries removal is to eliminate the diseased and necrotic tissues as well as any bacteria that may have the potential to cause persistent inflammation and treatment failure. Therefore, the total removal of the diseased dentin has a direct influence and impact on the clinical success of a restoration. However, the caries treatment techniques that are operated at the present time do not always or absolutely eradicate all of the microbes that are present in residual tissues) .Boston and Graver ,1994)

Effort at completely remove deep carious dentin using only mechanical techniques, may lead to risk of damaging the pulp of the tooth and/or causing extensive tooth structure loss.(de Almeida *et al*, 2011)

The strategy of caries removal using only mechanical methods are unsuccessful in producing a cavity that is absolutely free of caries (Cheng *et al*, 2013).Subsequently, coating the cavity preparation with antibacterial chemicals to aid in the eradication of microorganisms began to gain widespread favor among dental practitioners. (Al-Omari *et al*, 2006) The chemo mechanical caries removal system regarded as a substitute to the conventional caries removal with round bur in a slow speed hand piece. It is effective and comfortable, even it requires a longer time. (Ismail and Haidar, 2019)

In clinical dentistry, multiple disinfectants have been employed in an effort to lessen or eliminate microorganisms during cavity preparation and before to the insertion of dental restorations. Because of their inherent chemicals, some of these agents, has been noted to cause pulpal irritation. As a result, their use has been ignored (Shafiei and Memarpour, 2012)

The continuous search for more effective techniques of dental treatment has led to the investigation of a wide variety of lasers, and it has been shown that the capabilities of lasers in the field of dentistry are indeed advancing. The removal of dental hard tissue by laser has become both safer and more effective when used in conjunction with a water spray, and as a result, this technique is acquiring a larger amount of appreciation in the field of restorative dentistry. Erbium lasers, in particular, have the capability of removing enamel, dentin, and carious tissue with clear enamel-dentin boundaries and clean surfaces of enamel and dentin with different micro-morphologies. The morphology of lased dental surfaces presented homogeneous alterations. (Chowdhury *et al*, 2017)

In comparison to any other laser that is applied for dental purposes, the Er:YAG laser light has the highest absorption rate in water, and its wavelength matches well with the absorption maximum of hydroxyapatite.(DiVito *et al*, 2012)

A highly absorbed laser produces reactive oxygen species that damage the bacterial membrane, resulting in the rapid death of microorganisms. (Yao *et al*, 2012)

Laser energy has the potential to not only eliminate bacteria directly but also to stimulate the irrigant, thereby augmenting the bactericidal effects of the irrigant. (de Groot *et al* ,2009; Meire *et al* ,2009)

The Er:YAG laser triggered in a restricted volume of fluid, the high peak power derived from the short pulse duration combined with its high wavelength absorption in water , resulted in a photomechanical phenomenon (DiVito *et al*, 2012)). The term "photon induced photoacoustic streaming" is used to describe this phenomena (PIPS). (Sabreen and Hussien, 2021)

PIPS a new laser activated irrigation (LAI**)** process using a very low power source (subablative), pulses the laser light energy which absorbed by the irrigant molecules. This energy transfer generates a sequence of fast and violent shock waves able to pushing the irrigant through the entire root canal structure with great force. (DiVito *et al*, 2012)

Due to the fact that the bactericidal impact of pulsed Er:YAG laser is non-thermal, it is possible to avoid the unfavorable consequences of thermal energy. (Guidotti *et al*, 2012)

The purpose of the present study was to examine the bactericidal effect of erbium and chromium: dopped yttrium-scandium-gallium garnet (Er,Cr:YSGG) at short pulse duration (60 sec) using photon-induced photoacoustic streaming (PIPS).

2. Material and Methods

Antibacterial activity of test materials was estimated using Streptococcus mutans, provided by the Department of basic science, University of Baghdad. The techniques used in the research were the agar well technique and the tooth cavity model.

Agar well technique- Colombia blood agare was evenly distributed over the surface of 15 cm. in diameter petri dishes to a thickness of 5 mm. 0.5 ml. of *Streptococcus mutans* suspension (10^6 cfu/ml) was inoculated by a bent glass rod over the agar surfaces. Wells with a diameter of 4 mm were then punched into the agar using the blunt end of a sterile Pasteur pipette. The plates were then divided into three groups, each with seven plates. The well in the first group (I) loaded with 2% Chlorohexdine gluconate-based cavity disinfectant alone , in the second group (II) the well irradiated by erbium, chromium, yttrium, scandium, and gallium garnet laser (25 W, 15 Hz, 1% air, 1% water) using photon-induced photoacoustic streaming with short pulse duration (60 sec) .Lastly, chlorohexidine gluconate (2%CHX) was applied in the wells of the third group (III) then exposed to Er,Cr:YSGG laser radiation using the same setting stated above . Then the plate incubated at 37 C for 24 h. A sliding caliper was used to measure the diameter of the inhibition zone surrounding the wells in two randomly selected areas. The zone of inhibition (ZOI: mm) that appeared around the wells was recorded. *Tooth cavity model technique* - This part of the study was accomplished according to the manner used by Özer *et al* (Özer *et al, 2003*).

In order to complete this process, 28 human molars that were completely free of caries, restorations, and other flaws were used. In order to create flat dentin surfaces, the enamel of the teeth was amended horizontally with a water-cooled diamond bur to gain even dentin surfaces. Two cylindrical cavities 1mm in diameter, 2 mm depth) were prepared on the flat surface of each tooth without exposing the pulp as show in (Fig. 1).

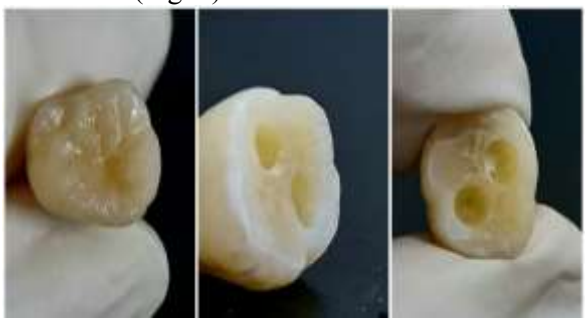

Figure (1): Preparation of the control and experimental cavities

The teeth were divided at random into four groups containing seven teeth (14 cavity preparations) each. The teeth were sterilized by autoclave for 15 minutes at a temperature of 121 ℃. The teeth kept in brain heart infusion (BHI) broth and incubated for 24 hours at 37°C, to confirm sterility. For washing out the culture medium and to avoid dehydration, each tooth was transferred in an individual tube hold 2 ml of sterile physiologic saline (SPS) and stored for 24 hours at 37°C. After that the teeth desiccated with sterile paper point and a gentle stream of air. To establish infected cavities, all the teeth were placed in a bottle containing broth culture of *Streptococcus mutans* suspension (10^6 CFU/ml) and incubated at 37°C for 72 hours. In group A the cavities were left untreated and served as the control. For Group B, the CHX 2% was applied into the cavities using a sterile brush, left undisturbed for one minute, and then it was gently dried with an air syringe. The experimental cavities in Group C treated using Er,Cr:YSGG laser (Waterlase, Biolase, California, USA) with 0.25 W , 1% water jet, and 1% air jet for a period of 30 seconds. In Group D, both 2% CHX based cavity disinfectant and Er,Cr:YSGG laser with the same parameter used above were applied to the experimental cavities.

Following the application of a temporary restorative material (Cavit GC) to the occlusal surfaces of the teeth, each tooth was placed in its own container of sterile physiological saline and stored at 37 ˚C for 72 hours. The teeth were then removed from the SPS, and standardized amounts of dentin chips (20 ± 5 mg) were collected from the cavity using a new sterile steel bur, mounted to a low-speed contra-angle hand piece, and then placed into sterile tubes. For every cavity, a new sterile bur was used to avoid overheating of dentinal walls during the cutting process. Adding 2 ml of sterile physiological saline into the suspensions with the dentin chips and mixed using Vortex for 30 seconds to enable the microorganisms to pass through the solution, thus produce a consistent suspension. Serial dilutions of 10−1, 10−2, and 10−3 were accomplished and the amount of S. mutans recovered was determined by plate count using Colombia blood agar.

Statistical analysis: Statistical analysis was carried out using one-way analysis of variance (ANOVA). LSD test was used to calculate the significant differences between tested mean, the letters (A, B and C) LSD represented the levels

of significant, highly significant started from the letter (A) and decreasing with the last one.

3. Result

For the agar well technique, the diameter of the inhibition zone in mm for each group is summarized in Table 1, which shows that group (III)where both Er,Cr:YSGG and CHX were used exhibited greatest diameter of inhibition zone). Group (I), 2% CHX alone, came in second. Er,Cr:YSGG laser group (II) showed the smallest inhibition zone diameter.

Table (1) Diameter of inhibition zones in mm measured in each group

Tested groups	N	Minimum	Maximum	Mean /mm	Std. Error	Std.D
Group I CHX	7	15.	22.	B 18.71	.94	2.49
Group II Laser	7	8.	12.	C 10.26	.56	1.49
Group III CHX+ laser	7	21.	32.	A 26	1.5	4.
P value	P0.001					

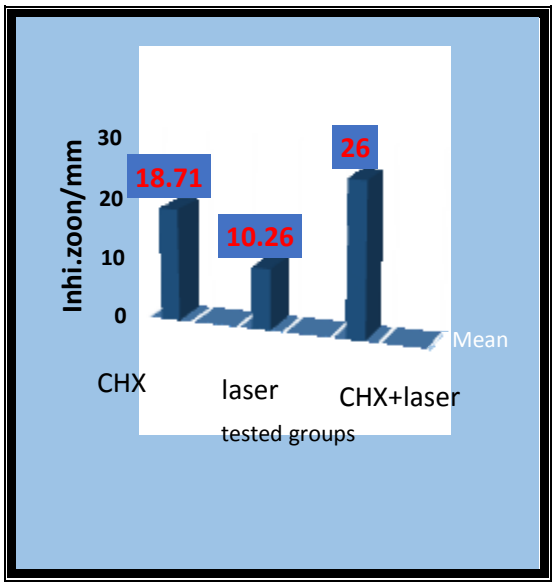

Figure (2) bar chart displays the inhibitory zone diameter for strep. mutans in millimeters

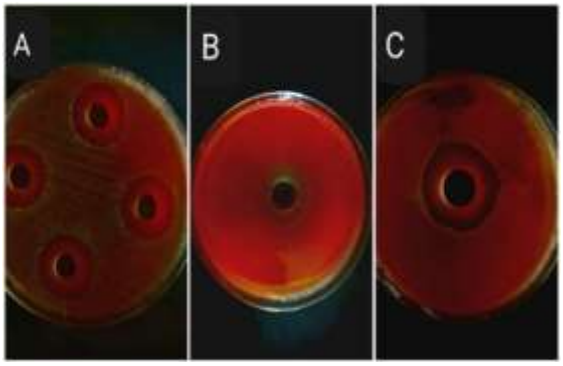

Figure (3) A) CHX, **B)** Laser and **C)** CHX+Laser

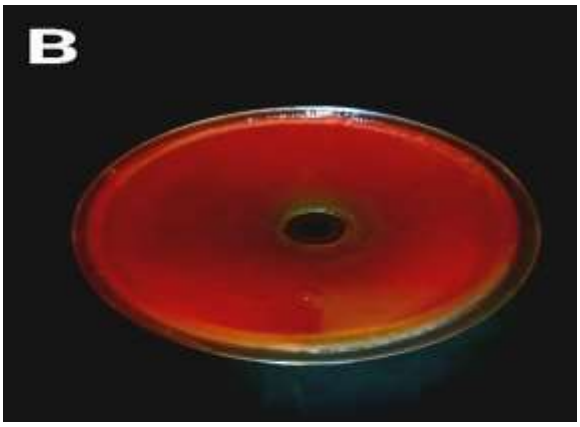

Figure(4) Inhibition Zone of Laser

Table 2 provides a summary of descriptive analysis regarding the number of thecovered bacteria across the groups. It demonstrates that the control group (A) had the highest mean percentage, which corresponds to the highest number of recovered bacteria. This was followed by group (B) which used 2% CHX as a cavity disinfectant, and finally by group (C) which utilised erbium laser alone. The activated erbium laser group with a 2% CHX group showed the lowest mean percentage, which was detected (D)

A) Conventional treatment, B) 2% chlorohexidine gloconate, C) Er,Cr:YSGG induced photoaccusic steaming, D) Er,Cr:YSG photoaccustic streaming with 2%CHX .

Table 2: Descriptive regarding the number of the covered bacteria across the groups.

Descriptive Statistics						
Tested groups	N	Minimum	Maximum	Mean		Std. Deviation
	Statistic	Statistic	Statistic	Statistic	Std. Error	Statistic
control before/***10^6**	7	.50	6.00	4.79	0.77	2.04
control after/***10^6**	7	10.00	22.00	13.14	1.74	4.60
CTX before/***10^6**	7	5.00	22.00	9.86	2.26	5.98
CTX after/***10^4**	7	.60	10.00	3.44	1.69	4.48
Laser before/***10^6**	7	10.00	20.00	13.86	1.71	4.53
Laser after/***10^3**	7	1.30	7.00	3.54	0.76	2.00
CHX+laser /before***10^6**	7	11.00	45.00	20.86	4.49	11.87
CHX+laser /after***10^2**	7	11.00	19.00	16.00	1.05	2.77

4. Discussion

In a recent study, the bactericidal impact of the Er,Cr:YSGG photon-induced photoacoustic streaming (PIPS) approach at short pulse duration (60 s) was investigated on the strain of Strep. Mutans. According to the results of the statistical analysis, the diameter of the inhibition zone was found to be highest in group D, which utilized both CHX and laser (table 1)

The primary reason may be that the chemical disinfectant absorbs laser energy, which results in the production of reactive oxygen species that disrupt the bacterial membrane (Yao *et al*, 2012). This, in turn, leads to an increase in the invasion of CHX particles into the bacteria, which ultimately results in the bacteria's death.

Because the laser beam is collimated and focusable, which means that all of the light rays or waves are travelling parallel to each other with the smallest divergence, the diameter of the inhibition zone in group C, where the Er,Cr:YSGG laser-induced photoacoustic streaming was used to inhibit the streptococcus mutants bacteria, is the smallest. This is because the laser beam is collimated and focusable (Menzel, and Photonics, 2013).

The descriptive statistics showed that the mean values of the percentage in the three experimental groups were lower than the control group. The percentage of CFU in group D where Er, Cr: YSGG photon induced photoacoustic streaming with 2% CHX was significantly high, followed by group C where Er,Cr:YSGG laser-induced photoacoustic streaming was used alone, while in group B that used CHX alone, less inhibition was observed than both Erbium laser groups (table 2).

In a previous study, the Er, Cr: YSGG laser was used at 0.75 and 1 W of output power and 20 Hz repetition rate, which produced statistically similar disinfectant potential in cavity walls to the use of chlorhexidine gluconate-based disinfectant solution (Turkun *et al*, 2006). However, in the current research, a better result was gotten in group C using the PIPS technique (table2), it could thus be assumed that the activation of CHX using PIPS by Er,Cr:YSGG laser provide the best antimicrobial activity compared to the conventional method .the main cause could be the photomechanical effect that occurs when the laser light energy is pulsed in a liquid (Sabreen and Hussien *et al* 2021; De Groot *et al*, 2009), When activation takes place in a liquid with minimal volume, the Er,Cr: YSGG frequency absorbed in water, with its peak power that after short pulse (60 sec), may be the reason for the observed photomechanical phenomenon. The resulted phenomenon was the reason for lowering the bacterial content of the treated cavities in group D, where the CHX agitated by erbium laser.

Based on the descriptive analysis, the group B with CHX only showed the lowest percentage of inhibition; this is because Berutti et al. (Berutti *et al*, 1997) found that chemical antimicrobials only reached 130 m into the dentin. In lab experiments, the length of time samples are inoculated has a direct impact on the depth of bacterial penetration. The cavities in the current investigation were only infected for 72 hours. This time frame is typically significantly longer in clinical situations, and the depth of bacterial penetration may even be greater than in our samples. In this regard, the deeper laser beam penetration depth provides a benefit in the removal of bacteria discovered in deeper layers of dentin during dental treatment.

The Er, Cr: YSGG laser was used in the current investigation with 600 um diameter glass tips (MZ6) and sub-ablative conditions (power of 0.25W, 15Hz, with 1% water and 1% air) at short pulse (60 sec). Before being exposing the teeth to laser radiation , rotary instruments were used for cavity preparation, that is because the laser parameter used in this study were significantly different from those typically used in clinical application due to the specific need of this microbiological investigation. The power output employed in this investigation to disinfect the cavities were lower than those used

for cavity preparation. Since the concentration of bacteria is highly sensitive to its diameter, the cavities prepared manually with round bur to guarantee that all of the cavities were of a uniform size. Additionally, water cooling aided by a water spray must be utilized cautiously to avoid the risk of transferring the microbes to other surfaces, since doing this will diminish the bacterial concentration inside the cavity and result in false negative results.

The antibacterial effect appears to be better than the conventional approach. Taking into account these factors, the bacterial inhibition was accomplished through photomechanical flowing of liquid as a result of laser activation rather than usual thermal vaporization. This light energy phenomenon is known as photon-induced photo acoustic streaming (PIPS), which produces shock waves. These shock waves are violent and very quick, which causes the bacterium cell wall to abruptly disintegrate.

In the current study the antibacterial effects of Er,Cr:YSGG laser and Concepsis(CHX) assessed by the cavity tooth model test designated by Özer et al. (Özer *et al ,2003*) .For the comparison of antibacterial activity of different materials, other antibacterial activity test models like the agar well and disc diffusion techniques considered to be inappropriate , as the diffusion rate of antibacterial solutions into the hydrophilic agar may differ meaningfully thus effecting the result. The cavity tooth model was developed to overawed these difficulties and to be able to compare materials by more accurate scientific reproductions, (Özer *et al, 2003*).

5. Conclusions

conclusion: From the extracted result, a photon-induced photoacoustic streaming technique employing an Er,Cr:YSGG pulsed laser (0.25 watts, 15 hertz, 1% air, and 1% water) at short pulse duration (60 microsecond) effectively agitates a chlorhexidine-based cavity disinfectant, which leads to the inhibition of Streptococcus Mutans.

References

Al-Omari WM, Al-Omari QD, Omar R. Effect of cavity disinfectionon postoperative sensitivity associated with amalgam. Operative dentistry, 2006, 31-2,165-170.

Berutti E, Marini R, Angeretti A. Penetration ability of different irrigants into dentinal tubules. J Endod 1997; 23: 725-727.

Boston DW, Graver HT. Histobacteriological analysis of acid red dye-stainable dentin found beneath intact amalgam restorations. Oper Dent 1994; 19: 65-69

Cheng L, Zhang K, Weir MD, Liu H, Zhou X, Xu HH. Effects of antibacterial primers with quaternary ammonium and nano-silver on *S. mutans* impregnated in human dentin blocks. Dent Mater 2013 Apr; 29(4):462-472.

Chowdhury, Sayan Roy; Marques,Márcia Martins ; Franzen, René ; Pedroni, Ana Clara Fagundes; Trevelin, Lívia Tosi; Abe, Gabriela Laranjeira; Gutknecht, Norbert (2017) Comparative ultrastructural analysis of Er:YAG laser scanner and conventional method for tooth cavity preparation.laser in dental science , 1(1),23-31.doi.1007/s41547-017-0003-2.

De Almeida Neves A, Coutinho E, Cardoso MV, Lambrechts P,Van Meerbeek B. Current concepts and techniques for caries excavation and adhesion to residual dentin. J Adhes Dent 2011 Feb; 13(1):7-22.

De Groot S.D. Verhaagen B. Versluis M. Wu M.K. Wesselink P.R., et al. Laser-activated irrigation within root canals: cleaning efficacy and flow visualization. Int. Endod. J. 2009; 42: 1077–1083. [PubMed] [Google Scholar].

DiVito E. Peters O.A. Olivi G. Effectiveness of the erbium:YAG laser and new design radial and stripped tips in removing the smear layer after root canal instrumentation. Lasers Med. Sci. 2012; 27: 273–280. [PubMed] [Google Scholar]

Guidotti R. Merigo E. Fornaini C. Rocca J.P. Medioni E., et al. Er:YAG 2,940-nm laser fiber in endodontic treatment: a help in removing smear layer. Lasers Med. Sci. 2012 Dec 5; [Epub ahead of print].

Ismail MM, Haidar AH. Impact of Brix 3000 and conventional restorative treatment on pain reaction during caries removal among group of children in Baghdad city .Journal of Baghdad College of Dentistry 31(2), 7-13, 2019.

Meire M.A. De Prijck K. Coenye T. Nelis H.J. De Moor R.J. Effectiveness of different laser systems to kill Enterococcus faecalis in aqueous suspension and in an infected tooth model. Int. Endod. J. 2009; 42:351–359. [PubMed] [Google Scholar]

Menzel, R., Photonics: linear and nonlinear interactions of laser light and matter. 2013: Springer Science & Business Media.

Özer F, Karakaya S, Ünlü N, Erganis O, Kav K, Imazato S. Comparison of antibacterial activity of two dentin bonding systems using agar well technique and tooth cavity model. *J Dent* 2003; 31: 111-116

Sabreen Sabah Rasheed, Hussien A Jawad, Radicular Dentine permeability Using Short Pulsed Er,Cr:YSGG laser with PIPS Technique, J Res Med Sci , 2021, 9(7):228-234

Shafiei F, Memarpour M. Antibacterial activity in adhesive dentistry: a literature review. Gen Dent 2012 Nov-Dec; 60(6): e346-e356.

S. S. Rasheed and H. A. Jawad .permeability of radicular dentine after using different irrigant Activation Technique including photon induce photoacoustic streaming technique, Iraqi J. Laser 20(1),43-50(2021)

TurkunM, Turkun LS, Celik EU, AtesM(2006) Bactericidal effect of Er,Cr:YSGG laser on Streptococcus mutans. Dent Mater J 25(1):81–86

Yao N. Zhang C. Chu C. Effectiveness of photoactivated disinfection (PAD) to kill enterococcus faecalis in planktonic solution and in an infected tooth model. Photomed. Laser Surg. 2012; 30: 699–704. [PubMed] [Google Scholar].

تطهير التجويف السني بأستخدام تقنية التدفق الضوئي – الصوتي المحتث بليزر الاربيوم – كروميوم

رند كريم جاسم , حسين علي جواد

معهد الليزر للدراسات العليا، جامعة بغداد، بغداد، العراق

الخلاصة

مقدمة: الهدف دراسة تأثير تقانة الري بالتدفق الصوتي - الضوئي المحتث بليزر الاربيوم – كروميوم في مدة النبضة القصيرة (٦٠ مايكروثانية) على عدد بكتريا المكورات العقدية الطافرة في المختبر.
المواد والطرق: تم استخدام ثمانية وعشرين ضرس ثالث مقلوع خالية من التسوس والشقوق والعيوب الأخرى. تم اختبار المواد باستخدام تقنية آجار جيدا ونموذج تجويف الأسنان. تمت تعبئة مواد الاختبار في آبار الألواح الملقحة بالعقدية الطافرة. بعد ٤٨ ساعة من الحضانة ، تم قياس مناطق المثبطات بالمليمترات. بالنسبة لاختبار نموذج تجويف الأسنان ، تم تحضير تجاويف أسطوانية في السطح الإطباقي المسطح للأسنان. تركت الأسنان في مزرعة مرق بكتريا المكورات العقدية الطافرة عند درجة ٣٧ درجة مئوية لمدة ٧٢ ساعة. ثم تم تقسيم الأسنان بشكل عشوائي إلى أربع مجموعات من سبعة أسنان (١٤ مجموعة تجويف) لكل منها. في المجموعة (أ) ، تُركت التجاويف التجريبية دون معالجة للسيطرة. في المجموعة (ب) ٢٪ مطهر تجويف قائم على الكلورهيكسيدين مطبق في تجاويف الزفير لمدة ٦٠ ثانية. في المجموعة (ج) تم استخدام ليزر الاربيوم – كروميوم (٠،٢٥واط، ١٥ هيرتز ، ١٪ هواء ، ١٪ ماء) بمدة نبضة قصيرة (٦٠ مايكرو ثانية). في المجموعة الأخيرة ، تم استخدام مطهر تجويف الكلورهيكسيدين لمدة٦٠ ثانية ثم الليزر لمدة ٣٠ ثانية بنفس المعلمة المذكورة أعلاه. ظلت الأسنان في محلول ملحي لمدة 72 ساعة. تم الحصول على كميات قياسية من رقائق العاج من جدران التجويف وتم حساب عدد البكتيريا المستعادة. النتيجة: تم تحليل النتيجة باستخدام اختبار ANOVAو .LSD بعد الاختبار الإحصائي، لوحظ فرق كبير في قطر منطقة التثبيط في المجموعة د (٢٦ مم) حيث تم استخدام كل من الكلورهيكسيدين والليزر متبوعًا بالمجموعة ب(١٨،٧١مم) حيث تم استخدام مطهر التجويف القائم على الكلورهيكسيدين. أقل فرق معنوي لوحظ في المجموعة ج (١٠،٢٦مم) حيث تم استخدام الليزر وحده. الخلاصة: بناءً على هذه الدراسة في المختبر ، فإن تقنية التدفق الضوئي الصوتي المحتث بالفوتون باستخدام الليزر الاربيوم -كروميوم (٠،٢٥ واط، ١٥ هيرتز، ١٪هواي، ١٪ ماء) عند مدة النبضة القصيرة (٦٠ مايكرو ثانية) يعمل على تحفيز مطهر التجويف القائم على الكلورهيكسيدين بشكل فعال مما يؤدي إلى تثبيط المكورات العقدية الطافرة.

Iraqi J. Laser, issue 2, vol., 21, pp. 48-57 (2022)

IRAQI JOURNAL OF LASER

Antimicrobial Photodynamic inactivation of using Rose Bengal and Low-Level Laser Light against *Staphylococcus aureus*

Qusay K. Abbas*, Layla M. Hassan

**Corresbonding author: qassi.khodair1202a@ilps.uobaghdad.edu.iq*
Institute of Laser for Postgraduate Studies.University of Baghdad.Baghdad.Iraq

(Received 9/9/2022; accepted 4/12/2022)

Abstract: Background: *Staphylococcus aureus* is Gram-positive bacteria that lives as a normal flora in living organisms but can be pathogenic to humans. Although a relatively unspectacular, nonmotile coccoid bacterium, *S. aureus* is a dangerous human pathogen in both community-acquired and nosocomial infections. Due to the increasing emergence of new strains of this antibiotic-resistant bacteria, it has become essential to approach different methods to control this pathogen. One of these methods is the antimicrobial photodynamic inactivation process using a low-level laser, in this paper, the Photodynamic effects of Rose Bengal and LLLL on the virulence factors of *S.aureus* were evaluated. **The aim of the study** The present study aims to evaluate the Photodynamic effects on *S. aureus* using laser irradiation and Rose Bengal as an external photosensitizer**. Methods:** sixty samples from sputum were taken. Then ten isolated from these samples were chosen to be under the study, where RB was used at a concentatin of 100 µg/ml that is activated by diode laser (532 nm) with power density of 1 W/m^{2}and exposure time (1, 2& 3) minute. **Results**: show that there is no effect on the inhibition of virulence factors except at the last minute, that is, the virulence factors decrease at the third minute only in the absence of a photosensitizer agent, while there is a direct effect of activated Rose Bengal on *S. aureus* isolated from the sputum of Iraqi patients with pneumonia, where all times of exposure of (RB + 532 nm) were effect on the virulence factors by inhibiting it. **Conclusions:** show that the diode laser of 532 nm has no effect on the virulence factor of *S. aureus* isolated from sputum except at the third minute, while RB activated by diode laser (532 nm) have an effective action on all virulence factors of *S. aureus* isolated from sputum at all times of exposure, accordingly, it was concluded that when using a laser diode alone, the bacterial viability decreases at the third minute only, While when using Rose Bengal activated by a diode laser, the viability of bacteria is reduced at all times of exposure.

Keywords: photodynamic effect; *Staphylococcus aureus*; Rose Bengal dye; photosensitizer

1. Introduction

S. aureus is Gram-positive bacteria that lives as a normal flora in living organisms but can be pathogenic to humans (Bien, Sokolova, & Bozko, 2011). Although a relatively unspectacular, nonmotile coccoid bacterium, *Staphylococcus aureus* is a dangerous human pathogen in both community-acquired and nosocomial infections. A fundamental biological property of this bacterium is its ability to asymptomatically colonize healthy individuals. *S. aureus* carriers are at higher risk of infection, and they are presumed to be an important source of the *S. aureus* strains that spread among individuals (Chambers & DeLeo, 2009). The pathogen can cause a wide variety of infections, which can be divided into three types: (i) superficial lesions such as wound infection, (ii) toxinoses such as food poisoning, scalded skin syndrome and toxic shock syndrome, and (iii) systemic and life-threatening conditions such as endocarditis, osteomyelitis, pneumonia, brain abscesses, meningitis, and bacteremia (Sousa, 2004).

The majority of staphylococci can spread illness in both anaerobic and aerobic environments. There are currently more than 80 species and subspecies in the genus, many of which can be located on mammalian mucous membranes and skin (Ahmed & Al-Daraghi 2022).

2. Virulence factors of *Staphylococcus aureus*

They are particles present or secreted by bacteria that play important and multiple roles in infection and pathogenesis, such as the colonization of the host cells, cell adhesion, and invasion of the host immune system. As well as inhibition of the host's immune response, several virulence factors possessed by Staphylococcal bacteria play an essential role in their pathogenesis (Jekle,Yoon, Zuck, Najafi, Wang, Shiau & Debabov, 2013).

3. Exoproteins

Some Staphylococci secrete a group of proteins, including Exotoxins and enzymes such as nuclease, protease, lipase & coagulase. Notably, the important goal of these proteins is to transform the local tissue of the host into a food substance used by the bacterial cell for growth (Dinges, Orwin, & Schlievert, 2000).

Hemolysins; Hole-forming toxins represent the most crucial group of toxins secreted by *S. aureus*. As these toxins break down red blood cells and release hemoglobin, the formation of pores or holes on the membranes of the host cell subject to the toxin leads to a loss of the integrity of the membrane by the formation of holes (Ratner, Hippe, Aguilar, Bender, Nelson & Weiser, 2006). This group is diverse and numerous, including alpha-hemolysin. It is the first bacteria exotoxin that has been identified among the hole-forming hemolytic toxins. It is a polypeptide with a molecular weight of (3302) KDa. This toxin disrupts the smooth muscle in blood vessels **(**Czajkowsky, Sheng, & Shao, 1998).

Proteases: *S. aureus* produces different types of protease, including metal protease, serine protease & cysteine protease. Many studies have suggested that these enzymes are essential virulence factors and that about 21% of the strains of these bacteria give areas of proteolysis on the casein agar medium. In contrast, the rest gives a negative result (Bose, Daly, Hall, Kenneth & Baylesa , 2014).

Dnase: A small globular protein composed of (149) amino acids with a molecular weight of (16.8) Kda and an optimal PH range between (8.6-10.3). It has recently been known that this enzyme is involved in the formation of the biofilm, as well as its contribution to the distribution and diffusion of that membrane and transmission or Subsequent promotion of bacterial propagation (Mann, Rice, Boles, Endres, Ranjit, Chandramohan, & Bayles, 2009).

Lipases: It is an enzyme known as FAME, which is produced by Staphylococci and harms the immune functions of the host, as all strains of *S. aureus* and more than 30% of other types of Staphylococci produce this enzyme, which breaks down lipids as a primary function to ensure the survival of bacteria in the Sebaceous area of the body.

The activity of this enzyme in Staphylococci was noticed in 1901, as there are strains of *S. aureus* that secrete

two types of this enzyme, one is Geh and the other is lipase, both of which are required for the analysis of fats and the breakdown of nutrients in favor of bacteria (Rollof, Braconier, Söderström, & Nilsson-Ehle, 1988). The laser was invented more than 60 years ago and developed very quickly, and its applications expanded to include biology, medical, chemical, technology, and other fields (Chopra & Chawla, 1992). laser light has unique properties like monochromaticity, high intensity, and low beam divergence (Wahhab, Mahdi, Faris & Altiafy, 2017). Numerous studies have proven that the bactericidal effect of a diode laser (810 nm) is based on thermal properties; furthermore, bacteria cannot develop resistance to laser exposure (Asnaashari, Ebad & Shojaeian, 2016). low-level laser therapy work by a photochemical mechanism in which photons from the laser source interact with cells that result in stimulation them or biochemical changes (Mohammed & Al-ameri, 2021). Anti-microbial PDT has been recognized for approximately one hundred years. Numerous significant variables affect the sensitivity of diverse microorganisms to photodynamics. Staphylococcus aureus is Gram-positive bacteria that live in a normal flora in living organisms but can be pathogenic to humans. Because changing the place will produce new strains of this antibiotic-resistant bacteria, it has become essential to approach different methods to control this pathogen. This method uses an antimicrobial photodynamic use process, which depends on the presence factor of photosensitizer and oxygen, which cause irreversible damage to bacteria cells. Antibiotic-resistant microorganisms are increasing at an alarming rate. Consequently, innovative antimicrobial strategies are required without delay. Photodynamic therapy (PDT) consolidates oxygen with light-activated photosensitizers (PS) to create cytotoxic species and tissue death (Dolmans, Fukumura & Jain 2003). Also PDT shows promise as a treatment for several cancerous and non-malignant disorders, using a photosensitizer that is targeted specifically in the targeted site and exposing the lesions to visible light to cause photodamage and consequent cell death (Abbas, Al-Taee & Mahmood, 2012).

4. Material and methods

Table (1) Ready Culture Media

Seq.	The name of the medium	manufacture	Purpose
1	Mannitol salt agar	Himedia	Selective medium for *S. aureus*
2	Nutrient agar	Himedia	for the growth of bacteria
3	Blood agar	Himedia	Hemolysis test medium
4	DNase test agar	MERCK	DNA degradation test medium
5	Nutrient broth	Himedia	For the growth of bacteria
6	Sugar fermentation medium	Himedia	Carbohydrate fermentation test medium
7	Lipid agar	Himedia	Lipolysis test medium
8	Protease agar	Himedia	Proteolytic test medium

4.1 Rose Bengal (photosensitizer)

In 100ml of distilled water, 0.01g of Rose Bengal powder was dissolved to produce stock with a 100g/ml concentration. Filtration was used to sterilize the solution through a 0.20µm syringe filter. The stock was kept in the dark till use. This dye was used to inhibit bacterial isolates (Sabbahi, Ben Ayed & Jemli, 2018).

4.2 Physiological Saline Solution

It was produced by solubilizing 0.85g of Na Cl in 100 ml of distilled water and sterilizing it in an autoclave.

4.3 Catalase reagent

The bacteria' susceptibility to the catalase enzyme production was examined using a 3 % concentration of hydrogen peroxide. It was stored in an opaque glass bottle protected from light (MacFaddin, 2000).

4.4 Cytochrome Oxidase Indicator
This reagent was made by dissolving (1) g of a substance (N, N, N, N Tetra methyl -p- phenylene di amine di hydrochloride) in (100) ml of distilled water and storing it in an opaque glass vial (Tang & Stratton 2006).

4.5 Gram Stain
The different between G-positive and G-negative bacteria.

4.6 The plasma used in the coagulase test
It was obtained from the blood bank in Baghdad either in the form of plasma or blood, where plasma is obtained by centrifuging at 3000 cycles per minute for 20 minutes, and a sterile syringe separates the plasma.

4.7 Samples collection
The collection of samples was conducted using tiny swabs. Sixty samples from sputum were taken. Ten isolated from these samples were chosen to be under the study.

4.8 Isolation of *S. aureus*
After patient samples were collected, they were cultivated in a selective media (mannitol salt) medium and incubated aerobically for 24hrs at 37℃. Then the plates of the medium were examined.

4.9 Identification of *S. aureus*
Microscopical and biochemical tests are used to identify bacteria.

4.10 Microscopically examination
In order to identify bacteria, microscopy and biochemical analysis are utilized.

A- Colonial morphologies
Colonial characteristics of *S. aureus* on the mannitol salt agar medium were examined by dissecting a microscope at a magnification of (X8). Where include colony shape, size, height, edges, color, and effect on the medium, such as hemolysis and fermentation of mannitol.

B- Cell morphologies
Cells arrangement, chain formation, and Gram staining for *S. aureus* were examined microscopically by the Gram stain method (Matar, 2004).

4.11 Catalase test
By removing a tiny sample of colonies from the agar with a sterile loop and combining them with a few drops of 3 percent H_2O_2 on a slide, the catalase activity of S. aureus was determined. The lack of bubble formation indicates the absence of enzyme catalase (Heinz & Mortimer 1981).

4.12 Cytochrome Oxidase Test
Colonies were evaluated by removing a small number of colonies from the plate with a sterile loop and mixing it with a few drops of Cytochrome Oxidase Indicator on a glass slide. The appearance of the violet color within (10-20) seconds is a positive result (Atlase, Brown, & Parks, 1995).

4.13 Coagulase test
The plasma coagulation enzyme was investigated using the tube method, where 0.8 ml of blood plasma was added to 0.2 Brain heart infusion broth medium inoculated with growing bacterial isolates at the age of (18-24) hours in small tubes. Furthermore, incubated for 4 hours at 37 degrees Celsius, during which coagulation occurred, indicating the test was positive. The tubes that did not show clotting were left at room temperature until the next day (Holt, Krieg, Sneath, Staley & William, 1994).

4.14 Carbohydrate Fermentation Test
The fermentation medium of sugars containing sugars such as the mannitol to be tested was inoculated with a bacterial culture at age (18-24) hours and incubated at 37°C for seven days with daily follow-up of the color. Changing the medium's color from red to yellow signifies a positive test (Mahon, Lehman & Manuselis, 2018).

5. Virulence factors

5.1 Blood hemolysis test

On a blood agar medium, the examined bacterial isolates were cultured for 24 hours at 37 ° C. Observation of plate decomposition is evidence of bacterial secretion of the Hemolysin enzyme (Mathai, Sindhu , Sulochana & Sathyabhama, 2003).

5.2 Lipase test

The bacterial colonies were inoculated on a lipid agar medium) by the planning method, the plates were left for 24 hours at 37°C. Observation of decomposition in dishes is evidence of bacterial secretion of lipase enzyme (Slifkin, 2000).

5.3 DNase test

The bacterial colonies were inoculated on a Toluidine blue DNA agar by the planning method, and the dishes were incubated at 37°C for 24 hours; the blue color of the medium turned pink, indicating that the bacteria secreted a nuclease enzyme that breaks down DNA into nucleotides that combine with the dye toluidine blue to form a pink color, meaning that the test is positive.

5.4 Protease test

The bacterial colonies were inoculated on a lipid agar medium by planning procedure. The plates were left for 24 hours at 37 degrees Celsius; observing decomposition in dishes is evidence of the bacterial secretion of protease Enzyme (Hynes & Tagg, 1985).

.

6. Laser Irradiation

6.1 Diode laser irradiation without Rose Bengal

One ml of A diluted bacterial suspension at $1*10^5$ CFU/ml concentration is put in each Eppendorf tube and exposed to a diode laser (532 nm) at different exposure times (1, 2, and 3) minutes (except one of these Eppendorf tubes did not expose to laser light in order to keep it as a control) with power density of 1 W/cm^2. The bacterial suspension in Eppendorf tubes was grown on nutrient agar and incubated aerobically for 24 hrs. The virulence factors were tested. The irradiation of bacteria by diode laser without Rose Bengal is shown in fig. (1)

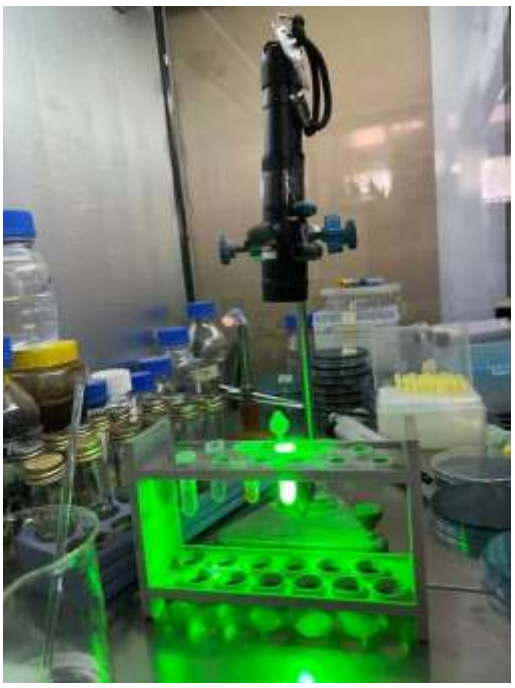

Figure (1): Irradiation of *S. aureus* by diode laser without Rose Bengal

6.2 Diode laser irradiation with Rose Bengal

Rose Bengal is considered a photosensitizer and has a maximum absorption at 550 nm, close to the wavelength of diode laser light, so it is chosen. Rose Bengal of 0.5 ml, with a 100 µg/ml concentration. It was added to these tubes containing bacterial suspension at a concentration of $1*10^5$ to get a final concentration equal to 50µg / ml. All these were exposed to laser light at different exposure times (1, 2, and 3) minutes, except one of the Eppendorf tubes did not expose to laser light (containing bacterial suspension and photosensitizer (Rose Bengal)) to act as a control. All bacterial suspensions in all tubes (exposed and non-exposed) were grown on nutrient agar for 24hrs at 37°C in an aerobic jar; then, the virulence factors were tested. The irradiation of bacteria by a diode laser with Rose Bengal is shown in fig. (2)

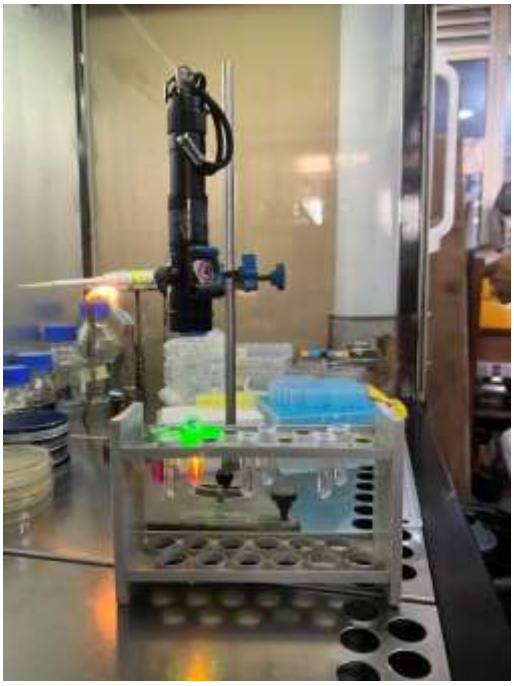

Figure (2): Irradiation of *S. aureus* by a diode laser with Rose Bengal

7. Statistical analysis

The statistical computer program IBM SPSS version 27.0 (IBM Corp. Released 2020) was used to calcultae the frequency and percentage frequency.

8. Results and Discussions:

8.1 Bacterial Identification

Two methods are used in the bacterial identification of three isolates of *S. aureus;* microscopic examination and biochemical tests.

8.2 Microscopic Examination

This method includes colonial morphologies and cell morphologies of *S. aureus*.

8.3 Colonial morphologies

In this study, under dissecting microscope, *S. aureus* that had grown on mannitol salt medium, where this medium is selective and differential because it contains a high percentage of salts (7.5-10) %, which can be tolerated by the genus *Staphylococcus,* as well as the medium contains mannitol sugar and mythel red reagent, as the bacteria of *S. aureus*. Yellow colonies with a diameter of (2-3) mm can ferment mannitol sugar and produce acidic products; consequently, the color of the medium changes from red to yellow (Leboffe & Pierce, 2019).

8. 4 Cell morphologies of *S aureus*

The S. aureus bacteria appeared through the microscopic examination of the slides stained with gram stain using the ordinary light microscope using an oil lens. Where the shape of the cells, their regularity, and the way they collect and interact with gram stain were observed. They are gram-positive cells with a spherical shape with a diameter of approximately 1µm, clustered in clusters, and they are in single spherical shapes, pairs, or quadrilaterals, and this corresponds to what was mentioned by (Matar, 2004) as shown in fig. (3).

8.5 Biochemical & culture factors tests

The results of diagnostic biochemical tests appeared similar for all ten isolates of *S. aureus* isolated from sputum, as shown in table (2)

Table (2) the results of diagnostic biochemical test

Type of test	Result
Suger Fermentation Test	+
Catalase test	+
Oxidase test	-
Coagulase test	+

8.6 Bacterial irradiation with Diode laser

One type of laser irradiated bacterial suspensions of ten isolates of *S. aureus*: diode laser.

This laser is a CW mode laser and emits light at 532 nm. Its output power was 80 mW, and its spot size was 1cm. The bacterial suspension was exposed for different exposure times (1, 2 & 3) minutes.

8.7 Virulence factors (without Rose Bengal)

8.7.1 Before and after irradiation

The virulence factors of *S. aureus* isolates as shown in the table (3):

Table (3) *S. aureus* virulence factors in sputum isolates without RB

Tests		Exposure time in minutes							
		0		1		2		3	
		N.	%	N.	%	N.	%	N.	%
Hemolysin	+Ve	10	100.0	10	100.0	10	100.0	6	60.0
	-Ve	0	0	0	0	0	0	4	40.0
Lipase	+Ve	10	100.0	10	100.0	10	100.0	4	40.0
	-Ve	0	0	0	0	0	0	6	60.0
Protease	+Ve	10	100.0	10	100.0	10	100.0	4	40.0
	-Ve	0	0	0	0	0	0	6	60.0
DNAse	+Ve	9	90.0	9	90.0	9	90.0	5	50.0
	-Ve	1	10.0	1	10.0	1	10.0	5	50.0

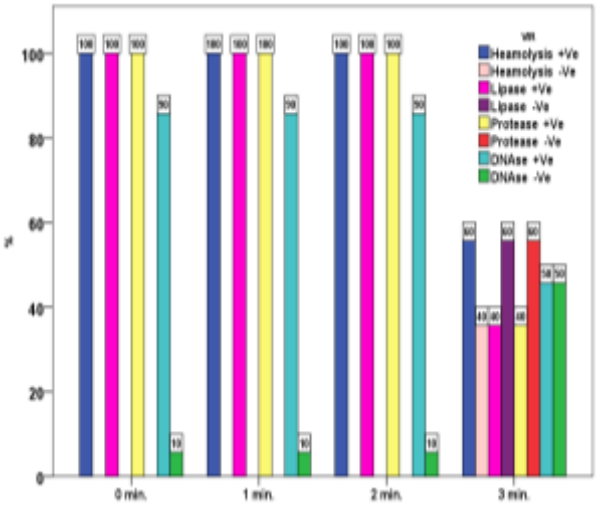

Figure (3): percentage frequency of *S. aureus* virulence factors in sputum isolates without RB

Statistical analysis of the results of bacterial irradiation by diode laser radiation without photosensitizer at different exposure time (1, 2& 3) minute, indicated that there is no effect on the inhibition of virulence factors except at the last minute, that is, the virulence factors decrease at the third minute only in the absence of a photosensitizer agent, the results agree with Fila and Grinholc's (Fila, Kawiak, & Grinholc, 2017).

The mechanism of action for the diode laser on virulence factors of *S. aureus* include the following:

When using a laser in range visible and near IR laser radiation occur one or more of the following physical and / or chemical changes can occur as a result of photoexcitation of their electronic state:

1-Alteration of redox properties and an acceleration of electron transfer, which can initiate of folding of protein and in this way influence the activity of the enzyme, as it was demonstrated for reduced cytochrome c. (important component of respiratory chain and can be considered as a primary photoacceptor) leads to inhibition in the manufacture of enzymes responsible for virulence factors.

2-during light excitation of electronic state, a noticeable fraction of the excitation energy is inevitably converted to heat, which causes a local transient increase in the temperature of the absorbing chromophres, this may cause structural (e.g. conformational) changes and trigger biochemical activity such as activation or inhibition of virulence factors enzymes,and the results of this study agree with many studies that used low-level laser, for instance, (DeSimone, Christiansenand Dore, 1999) the study showed the mechanisms of inhibiting virulence factors in *S. aureus* when using a low-level laser light.

8.7.2 Virulence factors (with Rose Bengal)

Before and after irradiation, The virulence factors of *S. aureus* isolates as shown in the table (4):

Table (4) *S. aureus* virulence factors in sputum isolates with RB

Test		Exposure time in minutes							
		0		1		2		3	
		N.	%	N.	%	N.	%	N.	%
Hemol-ysin	+	10	100.0	8	80.0	6	60.0	0	0
	-	0	0	2	20.0	4	40.0	10	100.0
Lipase	+	10	100.0	7	70.0	2	20.0	0	0
	-	0	0	3	30.0	8	80.0	10	100.0
Protease	+	9	90.0	6	60.0	3	30.0	1	10.0
	-	1	10.0	4	40.0	7	70.0	9	90.0
DNAse	+	9	90.0	5	50.0	3	30.0	0	0
	-	1	10.0	5	50.0	7	70.0	10	100.0

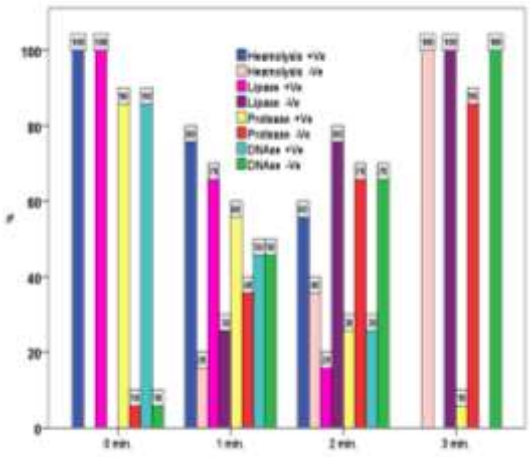

Fig. (4) percentage frequency of *S. aureus* virulence factors in sputum isolates with RB

Statistical analysis of the results that there are effects in the inhibition of virulence factors at all times of exposure in the presence of the photosensitizer agent (Tubby, Wilson & Nair, 2009).

The mechanism of action for the RB on virulence factors of *S. aureus* include the following:

1-The precise mechanism of inhibition of virulence factors may be due to the reactive oxygen species formed during photosensitization that can oxidize the proteins that make up the enzymes and thus disrupt their work.

2-The enzymes produced by the *S. aureus* bacteria, which are virulence factors that cause human diseases, have genes responsible for their secretion, such as *hlp, sspA*, *cidA,* and *gehA*. These genes encode beta-hemolysin, protease, Dnase, and lipase, respectively. Once Photodynamic action occurs through ROS generation, such as singlet oxygen (formed during the irradiation process), oxidative damage can occur to a variety of cellular components that play a significant role in the maintenance of bacterial stability, such as the structures of genes encoding enzymes and molecular components (proteins and lipids) of external structures. This alteration in the structures of genes encoding enzymes inhibits the enzymes, ,and the results of this study agree with many studies that used low-level laser with appropriate quantity of the photosensitizer, for instance, (Bartolomeu, Rocha, Cunha, Neves, Faustino, & Almeida, 2016) the objective of this work was to evaluate the effect of antimicrobial photodynamic inactivation (PDI) on virulence factors of *S. aureus* and to assess the potential development of resistance of this bacterium as well as the recovery of the expression of the virulence factors after successive PDI cycles, and the PDI process is based in the combined use of light, oxygen, and an intermediary agent (a photosensitizer)

9. Conclusions

1-The diode laser of 532 nm has no effect on the virulence factor of *S. aureus* isolated from sputum except at the third minute.

2-Rose Bengal activated by diode laser (532 nm) have an effective action on all virulence factors of *S. aureus* isolated from sputum at all times of exposure.

3- Accordingly, it was concluded that when using a laser diode alone, the bacterial viability decreases at the third minute only, but when using a diode laser in the presence of RB, the bacterial viability decreases at all times of exposure.

References

Abbas, R. S., Al-Taee, E. H., & Mahmood, A. S. (2012). Photodynamic Therapy for Leiomyosarcoma: In vitro study. *Iraqi Journal of Laser*, *11*(B), 1-7.

Ahmed, Z. F., & Al-Daraghi, W. A. H. (2022). Molecular Detection of medA Virulence Gene in Staphylococcus aureus Isolated from Iraqi Patients. *Iraqi journal of biotechnology*, *21*(1).

Asnaashari, M., Ebad, L. T., & Shojaeian, S. (2016). Comparison of antibacterial effects of 810 and 980-nanometer diode lasers on enterococcus faecalis in the root canal system-an in vitro study. *Laser therapy*, *25*(3), 209- 214.

Atlase , R. M. ; Brown , A. E. & Parks , L. C. (1995). Laboratory Manual Experimental Microbiology. Mosby-Comp:119-121.

Bien, J., Sokolova, O., & Bozko, P. (2011). Characterization of virulence factors of Staphylococcus aureus: novel function of known virulence factors that are implicated in activation of airway epithelial proinflammatory response. *Journal of pathogens*, *2011*.

Bartolomeu, M., Rocha, S., Cunha, Â., Neves, M. G. P. M. S., Faustino, M. A., & Almeida, A. (2016). Effect of photodynamic therapy on the virulence factors of Staphylococcus aureus. *Frontiers in Microbiology*, *7*, 267.

Bose , J. L. ; Daly , S. M. ; Hall , P. R. ; Kenneth W. & Baylesa , K. W. (2014). Identification of the *Staphylococcus aureus* vfrAB Operon, a Novel Virulence Factor Regulatory Locus. 82 (5) : 1813–1822.

Chambers, H. F., & DeLeo, F. R. (2009). Waves of resistance: Staphylococcus aureus in the antibiotic era. *Nature Reviews Microbiology*, *7*(9), 629-641.

Chopra, S; Chawla, H.M. (1992): Laser in chemical and Biological Sciences. Wiely Eastern limited pub co.

Czajkowsky, D. M., Sheng, S., & Shao, Z. (1998). Staphylococcal α-hemolysin can form hexamers in phospholipid bilayers. *Journal of molecular biology*, *276*(2), 325-330

DeSimone, N.J; Christiansen, C. and Dore, D. (1999): Bactericidal effect of 0.95 mw He – Ne and 5mw Indium- Gallium-Aluminum- phosphate Laser irradiation at exposure times of 30,60 and 120 seconds of photosensitized *Staphylococcus aureus* and *Pseudomonas aeroginosa* in vitro physical therapy vol. 79 no. 9.

Dinges, M. M., Orwin, P. M., & Schlievert, P. M. (2000). Exotoxins of Staphylococcus aureus. *Clinical microbiology reviews*, *13*(1), 16-34.

Dolmans, D. E., D. Fukumura, and R. K. Jain**.** **(**2003). *Photodynamic therapy for cancer*. Nat. Rev. Cancer 3**:**380-387**).**

Fila, G., Kawiak, A., & Grinholc, M. S. (2017). Blue light treatment of Pseudomonas aeruginosa: Strong bactericidal activity, synergism with antibiotics and inactivation of virulence factors. *Virulence*, *8*(6), 938-958

Heinz, S. and Mortimer, P.S. (1981); Principles of isolation, cultivation and conservation of bacteria in: Mortimer, P.S;

Heinz, S; Hans, G.T: Albert, B. and Hans, G.S. vol.1. Springer-verlag Brlin Heidalbergy. Newyork. pp:135-175

Holt , J. G. ; Krieg , N. R. ; Sneath , P. H. ; Staley , J. T. & William , S.T. (1994). Broad of trustees of Berg's manual of determinative bacteriology .9th ed. ,Williams and Wilkins publication .Baltimor .pp:42-43.

Hynes, W. L., & Tagg, J. R. (1985). A simple plate assay for detection of group A streptococcus proteinase. *Journal of microbiological methods*, *4*(1), 25-31.

IBM Corp. Released 2020. IBM SPSS Statistics for Windows, Version 27.0. Armonk, NY: IBM Corp.

Jekle, A., Yoon, J., Zuck, M., Najafi, R., Wang, L., Shiau, T., ... & Debabov, D. (2013). NVC-422 inactivates Staphylococcus aureus toxins. *Antimicrobial agents and chemotherapy*, *57*(2), 924-929.

Leboffe, M. J., & Pierce, B. E. (2019). *Microbiology: Laboratory Theory and Application, Essentials*. Morton Publishing Company.

MacFaddin , J. F. (2000). Biochemical Tests for Identification of Medial Bacteria. 3rd ed., Lippincott Williams and Wikins,a walters Kluwer Com., London. pp:484-485.

Mahon, C. R., Lehman, D. C., & Manuselis, G. (2018). *Textbook of diagnostic microbiology-e-book*. Elsevier Health Sciences.

Mann, E. E., Rice, K. C., Boles, B. R., Endres, J. L., Ranjit, D., Chandramohan, L., ... & Bayles, K. W. (2009). Modulation of eDNA release and degradation affects Staphylococcus aureus biofilm maturation. *PloS one*, *4*(6), e5822.

Matar, S. (2004). *Characterization of staphylococcal small colony variants and their pathogenic role in biomaterial-related infections with special reference to staphylococcus epidermidis* (Doctoral dissertation, University of Nottingham).

Mathai , J. ; Sindhu , P. N. ; Sulochana , P. V. & Sathyabhama , S. (2003). Haemolysin test for characterization of immune ABO antibodies. Indian J. Med Res 118 : 125-128

Mohammed, S. E., & Al-ameri, L. M. (2021). Laser Biostimulation Effect on Human Sperm Motility. *Iraqi Journal of Laser*, *20*(1).

Sousa, M. A. D. H. D. Lencastre (2004)"Bridges from hospitals to the laboratory: genetic portraits of methicillin-resistant Staphylococcus aureus clones". *FEMS Immunology and Medical Microbiology*, 101-111.

Wang ,Y. & Stratton , C. W. (2006). Advanced Techniques in DiagnosticMicrobiology. Springer Science Business Media , LLC. Printed in the United States of America

Tubby, S., Wilson, M., & Nair, S. P. (2009). Inactivation of staphylococcal virulence factors using a light-activated antimicrobial agent. *BMC microbiology*, *9*(1), 1-10.

Wahhab, H. K., Mahdi, Z. F., Faris, R. A., & Altiafy, D. O. (2017). Laser Enhanced Photocatalyic Degradation of Methylene blue using Nanostructured ZnO Catalyst based on Interfacial Charge Transfer. *Iraqi Journal of Laser*, *16*(A), 25-30.

Ratner, A. J., Hippe, K. R., Aguilar, J. L., Bender, M. H., Nelson, A. L., & Weiser, J. N. (2006). Epithelial cells are sensitive detectors of bacterial pore-forming toxins. *Journal of Biological Chemistry*, *281*(18), 12994-12998.

Rollof, J., Braconier, J. H., Söderström, C., & Nilsson-Ehle, P. (1988). Interference of Staphylococcus aureus lipase with human granulocyte function. *European Journal of Clinical Microbiology and Infectious Diseases*, *7*(4), 505-510.

Sabbahi, S., Ben Ayed, L., & Jemli, M. (2018). Staphylococcus aureus photodynamic inactivation mechanisms by rose bengal: use of antioxidants and spectroscopic study. *Applied Water Science*, *8*(2), 1-9.

Slifkin, M. (2000). Tween 80 opacity test responses of various Candida species. *Journal of Clinical Microbiology*, *38*(12), 4626-4628

التأثير الديناميكي الضوئي لروزالبنغال المنشط بواسطة ضوء ليزر منخفض المستوى على *S. aureus*

قصي خضير عباس ليلى محمد حسن

معهد الليزر للدراسات العليا . جامعة بغداد . بغداد . العراق

الخلاصة: المكورات العنقودية الذهبية هي بكتيريا موجبة الجرام تعيش كفلورا طبيعية في الكائنات الحية ولكنها يمكن أن تكون مسببة للأمراض للإنسان. على الرغم من كونها بكتيريا كروية غير متحركة نسبيًا ، إلا أن المكورات العنقودية الذهبية هي أحد مسببات الأمراض الخطيرة البشرية في كل من العدوى المكتسبة من المجتمع واصابات المستشفيات. نظرًا لتزايد ظهور سلالات جديدة من هذه البكتيريا المقاومة للمضادات الحيوية ، فقد أصبح من الضروري اتباع طرق مختلفة للسيطرة على هذا العامل الممرض. إحدى هذه الطرق هي عملية التعطيل الضوئي الديناميكي المضاد للميكروبات باستخدام ليزر منخفض المستوى ، في هذا البحث ، تم تقييم التأثيرات الديناميكية الضوئية لروز البنغال وضوء الليزر منخفض المستوى على عوامل ضراوة *S. aureus* تم أخذ ستين عينة من البلغم. ثم تم اختيار عشر عينات معزولة من هذه العينات لتكون قيد الدراسة ، حيث تم استخدام روز البنغال بتركيز 100 ميكروغرام / مل يتم تنشيطه بواسطة ليزر الصمام الثنائي (532 نانومتر) بجرعات مختلفة (6،12 و 18) جول / سم 2. أظهرت النتائج أنه لا يوجد تأثير على تثبيط عوامل الضراوة إلا عند كثافة الطاقة الأخيرة (18 جول / سم 2) ، أي أن عوامل الضراوة تنخفض عند كثافات الطاقة العالية فقط في حالة عدم وجود عامل متحسس ضوئي. بينما كان هناك تأثير مباشر لعقار روز البنغال المنشط على بكتيريا *S. aureus* المعزولة من بلغم المرضى العراقيين المصابين بالالتهاب الرئوي ، حيث أثرت جميع الجرعات (532 نانومتر+ روز البنغال) على عوامل الضراوة عن طريق تثبيطها. أظهرت النتائج أن ليزر الصمام الثنائي البالغ 532 نانومتر ليس له أي تأثير على عوامل ضراوة *S. aureus* المعزولة من البلغم إلا بجرعات عالية ، بينما روز البنغال المنشط بواسطة ليزر الصمام الثنائي (532 نانومتر) له تأثير فعال على جميع عوامل ضراوة *S. aureus*المعزولة من البلغم في جميع الجرعات (6،12 و 18 جول / سم 2) ، وبناءً عليه ، استنتج أنه عند استخدام الصمام الثنائي ليزر لوحده ، تقل قابلية بقاء البتكريا بالجرعات العالية فقط ، ولكن عند استخدام روز البنغال المنشط بواسطة ليزر ثنائي الصمام تنخفض قابلية بقاء البكتيريا في جميع الجرعات